



Chemical and boron isotope composition of tourmaline from the Kiaka orogenic gold deposit (Burkina Faso, West African Craton) as a proxy for ore-forming processes

J. Gauriau, M. Harlaux, Anne-Sylvie André-Mayer, A. Eglinger, A. Richard, A. Fontaine, M.G. Lefebvre, D. Béziat, J. Villeneuve, D. Lemarchand

► To cite this version:

J. Gauriau, M. Harlaux, Anne-Sylvie André-Mayer, A. Eglinger, A. Richard, et al.. Chemical and boron isotope composition of tourmaline from the Kiaka orogenic gold deposit (Burkina Faso, West African Craton) as a proxy for ore-forming processes. *Mineralium Deposita*, 2020, 10.1007/s00126-020-01002-7 . hal-02958894

HAL Id: hal-02958894

<https://hal.univ-lorraine.fr/hal-02958894>

Submitted on 12 Oct 2020

HAL is a multi-disciplinary open access archive for the deposit and dissemination of scientific research documents, whether they are published or not. The documents may come from teaching and research institutions in France or abroad, or from public or private research centers.

L'archive ouverte pluridisciplinaire **HAL**, est destinée au dépôt et à la diffusion de documents scientifiques de niveau recherche, publiés ou non, émanant des établissements d'enseignement et de recherche français ou étrangers, des laboratoires publics ou privés.

Chemical and boron isotope composition of tourmaline from the Kiaka
orogenic gold deposit (Burkina Faso, West African Craton) as a proxy
for ore-forming processes

J. Gauriau ^{1,2*}, M. Harlaux ³, A.-S. André-Mayer ^{1*}, A. Eglinger ¹, A. Richard ¹, A. Fontaine ⁴,
M.G. Lefebvre ⁵, D. Béziat ⁶, J. Villeneuve ⁷, D. Lemarchand ⁸

¹ Université de Lorraine, CNRS, GeoRessources, F-54000 Nancy, France

² Present address: Department of Earth Sciences, University of Southern California, Los
Angeles, CA 90089-0740, USA

³ Nevada Bureau of Mines and Geology, University of Nevada, Reno, NV 89557-0178, USA

⁴ Institut National de la Recherche Scientifique (INRS), 490 rue de la couronne, G1K 9A9,
Quebec City, QC, Canada

⁵ GFZ German Research Centre for Geosciences, Telegrafenberg, 14473 Potsdam, Germany

⁶ Géosciences Environnement Toulouse (GET), Université Paul Sabatier, CNRS, IRD, 14
Avenue Edouard Belin, 31400 Toulouse, France

⁷ Centre de Recherches Pétrographiques et Géochimiques (CRPG), CNRS-Université de
Lorraine, 15 rue Notre-Dame des Pauvres, 54501 Vandœuvre-lès Nancy, France

⁸ Laboratoire d'Hydrologie et de Géochimie de Strasbourg (LHYGES), Université de
Strasbourg-EOST, CNRS, ENGEES, 1 rue Blessig, 67084 Strasbourg Cedex, France

* Corresponding authors: anne-sylvie.andre@univ-lorraine.fr, gauriau@usc.edu

Abstract

The Kiaka orogenic gold deposit (Burkina Faso), located in the Paleoproterozoic domain of the West African Craton, is characterized by a two-stage gold mineralization hosted in volcano-sedimentary metamorphic rocks that was formed during the Eoeburnean (2.20-2.13 Ga) and Eburnean (2.13-2.05 Ga) orogenic cycles. These two stages include an early disseminated low-grade gold mineralization and a late vein-hosted high-grade gold mineralization. A paragenetic study indicates that the first gold stage was coeval with the deposition of hydrothermal tourmaline. The aim of this paper is twofold: (i) to determine the processes responsible for the economic disseminated gold mineralization, and (ii) to identify the source of the mineralizing fluids. To this end, we combine *in situ* analyses obtained from electron probe microanalysis and secondary ion mass spectrometry measurements. A dravite composition characterizes the hydrothermal tourmaline hosted in metamafic volcanic rocks and metagreywackes, and $\delta^{11}\text{B}$ values range within the two intervals [-25.1‰; -22.0‰] and [-19.6‰; -15.1‰]. Our results suggest that tourmaline formed from a high-temperature (ca. 400°C), reduced, and low-salinity hydrothermal fluid that interacted with the local host rocks. From the modeling of tourmaline-fluid boron isotope fractionation, we infer a metamorphic fluid origin derived from devolatilization of deeply-buried muscovite schists during the regional prograde to peak metamorphism prior ca. 2.13 Ga. This metamorphic fluid-rock interaction model may possibly extend to other orogenic gold deposits in the West African Craton.

Keywords

Tourmaline, Boron isotopes, Orogenic gold deposit, West African Craton, Burkina Faso.

INTRODUCTION

Tourmaline is the most important borosilicate mineral on Earth and represents a reliable monitor of the physico-chemical conditions of the environment in which it crystallized due to three main properties: (i) it is a stable mineral over a large range of pressure and temperature conditions, (ii) it has a complex crystal chemistry incorporating a large range of chemical elements, and (iii) it shows negligible intracrystalline diffusion, making it an excellent petrogenetic indicator for determining fluid sources and processes (Dutrow and Henry 2011; Slack and Trumbull 2011; van Hinsberg et al. 2011). Tourmaline is a common mineral in orogenic gold deposits worldwide, often found disseminated in gold-bearing quartz veins or as metasomatic replacements along the host rock vein selvages. Deposition of tourmaline and gold is generally interpreted to be synchronous (King and Kerrich 1989; Mueller et al. 1991; Kotzer et al. 1993; Anglin et al. 1996; Frei and Pettke 1996; Slack 1996; Rowins et al. 1997; Jiang 1998; Béziat et al. 1999), suggesting that tourmaline can be used as a proxy for tracing the ore-forming processes.

Fluid and metal sources in orogenic golds deposits, including Au and B, are still debated, therefore a large diversity of genetic models have been proposed. This diversity may either reflect an intrinsic variability of orogenic gold deposits or may show divergence between interpretations. The current paradigm for the formation of orogenic gold deposits involves a metamorphic fluid derived from devolatilization of thick metasedimentary sequences during prograde to retrograde metamorphic evolution of greenstone belts (e.g. Wyman and Kerrich 1988; Goldfarb et al. 2005; Phillips and Powell 2010; Goldfarb and Groves 2015; Fusswinkel et al. 2017; Groves et al. 2019). Alternatively, a magmatic origin for fluids and metals related to reduced intrusions has been proposed (Burrows and Spooner 1987; Wang et al. 1993; Tomkins 2013; Xue et al. 2013), as well as mixed magmatic-metamorphic fluid origins (Rogers

et al. 2013; Molnár et al. 2016). The source of boron in orogenic gold environments may be derived from (i) metamorphic fluids produced during devolatilization reactions of metasedimentary sequences that occur above 650°C (Spear et al. 1999; van Hinsberg et al. 2011), and/or (ii) magmatic fluids released from boron-rich reduced magmas (Trumbull and Slack 2018). In previous studies, tourmaline has been used as a proxy for (i) to identify trace elements that discriminate tourmaline from gold-bearing veins from orogenic gold deposits (Sciuba et al. 2020), (ii) tracing the origin of hydrothermal fluids and metals (distal vs. proximal; metamorphic vs. magmatic) and for (iii) determining the ore-forming processes yielding to deposition of gold, such as in the Yilgarn craton (Jiang et al. 2002), the Archean Abitibi belt (King and Kerrich 1989; Beaudoin et al. 2013), the Archean Barberton greenstone belt (Byerly and Palmer 1991), the Archean Hattu schist belt (Molnár et al. 2016), the Hutti-Maski Greenstone Belt (Hazarika et al. 2015), and the Paleoproterozoic West African Craton (Lambert-Smith et al. 2016; this study).

The Kiaka orogenic gold deposit (Burkina Faso) is hosted in the Manga Fada N’Gourma Paleoproterozoic greenstone belt, located on the southeast domain of the West African Craton. The regional host rocks consist of metavolcanic and metasedimentary units composed of metapelites, greywackes, and schists. A dioritic pluton dated at 2140 ± 7 Ma (Fontaine et al. 2017) intruded the schists contemporaneously with a regional shearing event. The Kiaka deposit contains a polyphase gold mineralization formed between ca. 2150 Ma and 2080 Ma that is interpreted to be coeval with the deposition of hydrothermal tourmaline (Fontaine et al. 2017; Le Mignot et al. 2017). This paper provides new data on the chemical and boron isotopic composition of hydrothermal tourmaline, as well as whole-rock boron isotope composition of the host rocks. The objective is to trace the ore-forming processes and the origin of mineralizing fluids in the Kiaka gold deposit, focusing specifically on hydrothermal tourmaline associated to the ca. 2150 Ma disseminated gold mineralization. The origin of the mineralizing fluids is

discussed relative to the two potential sources: the dioritic intrusion (magmatic origin) and the metasedimentary rocks (metamorphic origin).

GEOLOGICAL CONTEXT

The Paleoproterozoic Baoulé-Mossi domain

The Paleoproterozoic southern part of the West African Craton (WAC) is composed of low-grade volcanic and volcano-sedimentary Birimian rocks (ca. 2.20-2.14 Ga) and siliciclastic sediments (ca. 2.13-2.09 Ga) that were intruded by voluminous granites (Grenholm et al. 2019). The oldest Birimian sequence consists of tholeiitic basalt, gabbro, pyroxenite, and minor calc-alkaline ultramafic-mafic to differentiated suites (Baratoux et al. 2011). The geodynamic context of formation of the Birimian rocks remains unclear and several interpretations have been proposed, including a plume-related oceanic plateau (Abouchami et al. 1990; Boher et al. 1992; Augustin and Gaboury 2017) and an oceanic context evolving from a MORB-like domain to an increasingly mature volcanic arc domain (Pouclet et al. 2006; Baratoux et al. 2011; Labou et al. 2020). This period characterizes the Eoeburnean cycle, defined by an early magmatic accretion stage followed by an arc construction stage in a convergent setting (Baratoux et al. 2011; McFarlane et al. 2019). The Eburnean orogenic cycle started with the filling of major sedimentary basins by flysch sequences derived from the erosion of the Birimian crust and their inversion between ca. 2.13 Ga and 2.10 Ga (Davis et al. 2015; Grenholm et al. 2019). Different depositional settings have been proposed such as syn-orogenic foreland basin sedimentation (Feybesse et al. 2006; Block et al. 2016) or back-arc and fore-arc basin sedimentation controlled by extensional detachments (Perrouy et al. 2012; Grenholm et al. 2019). The paroxysm of the Eburnean cycle is characterized by tectonic accretion and crustal reworking between ca. 2.09 and 2.05 Ga (e.g. Masurel et al. submitted). Large transpressional shear zones cross-cut the

Baoulé-Mossi domain contemporaneously with the emplacement of high-K calc-alkaline to shoshonitic granitic plutons (Feybesse and Milési 1994; Egal et al. 2002; Parra-Avila et al. 2019) in syn- to post-collisional settings (Eglinger et al. 2017; Masurel et al. 2017; Thébaud et al. 2020).

Paleoproterozoic gold metallogeny of the Baoulé-Mossi domain

West Africa is currently the largest Paleoproterozoic gold-producing region in the world with an annual gold production of ca. 250 t (Béziat et al. 2008; Markwitz et al. 2016; Robertson and Peters 2016; Goldfarb et al. 2017). The majority of gold deposits are closely located to major first-order tectonic structures such as the Markoye shear zone (MSZ, Fig. 1A) in Burkina Faso (Tshibubudze and Hein 2013), the Ashanti shear zone (AS, Fig. 1A) in Ghana (Perrouy et al. 2012) and the Senegal-Mali shear zone (Ledru et al. 1991, Lawrence et al. 2013) that affected greenstone belts. Gold deposits in the southern WAC formed during the long-lived period of a magmatic accretion stage, defined as the Eoeburnean cycle, and broadly during the reworking and tectonic accretion stages of the Eburnean orogenic cycle (Masurel et al. submitted). Few absolute, and some relative ages constrain gold mineralization between ca. 2.18 and 2.06 Ga, and a few are linked to polyphase mineralization processes (such as the Obuasi Au deposit; Fougrouse et al. 2017; Le Mignot et al. 2017; Augustin et al. 2017). The oldest orogenic gold deposits are mostly known in the eastern part of the Baoulé-Mossi domain, formed during the Eoeburnean deformation between ca. 2.14 and 2.13 Ga (Lawrence et al. 2017; Le Mignot et al. 2017). They include the ~5.8 Moz Kiaka gold deposit, hosted by volcano-sedimentary rocks which were deformed and metamorphosed under amphibolite facies conditions (Fontaine et al. 2017). Early Eburnean gold deposits (ca. 2.11-2.09 Ga) correspond to different types of gold deposits including orogenic (Obuasi deposit; Fougrouse et al. 2017), conglomerate-hosted paleo-placer (Tarkwa deposit; Perrouy et al. 2012), granitoid-hosted (Chirano deposit;

Allibone et al. 2004), intrusion-related (Morila deposit; McFarlane et al. 2011), and skarn (Tongon deposit; Lawrence et al. 2017) gold deposits. Some gold deposits formed during the late Eburnean tectono-thermal activity between ca. 2.09 and 2.05 Ga following docking of the Archean and Paleoproterozoic domains within the southern WAC, synchronous with widespread high-K and shoshonitic granites (Eglinger et al. 2017; Masurel et al. 2017). Economic gold mineralization associated with this transcurrent tectonics and crust-derived magmas are widespread in the western portion of the Baoulé-Mossi domain (Thébaud et al. 2020; Masurel et al. submitted).

Local geology and structural framework of the Kiaka deposit

The Kiaka orogenic gold deposit is located within an elongated volcano-sedimentary sequence known as the Manga Fada N’Gourma greenstone belt, which extends along 250 km from northeast to southwest (Hottin and Ouégrago 1976; Naba et al. 2004; Ganne et al. 2012). The deposit is located at the intersection between two major structures, the Markoye Shear Zone (MSZ) and a D2-related NE-trending shear zone (Fig. 1A-B; Fontaine et al. 2017). The volcano-sedimentary sequence hosting the Kiaka deposit forms a NE-striking corridor, strongly dipping to the northwest and commonly subparallel to the regional foliation (Fig. 1B). Host rocks consist of conglomerate, metagreywacke, and metapelite, which are intercalated with garnet-orthopyroxene schists and mafic rocks (Fontaine et al. 2017). Several magmatic rocks have been described in the Kiaka area, such as a biotite-amphibole diorite plug dated at 2140 ± 7 Ma (Fontaine et al. 2017) and an unfoliated biotite granite, dated between 2120 and 2100 Ma, intruding the tonalite-trondhjemite-granodiorite (TTG) basement (Castaing et al. 2003; Vegas et al. 2008; Fontaine et al. 2017). Lithogeochemical data suggest similarities between the biotite-amphibole diorite and the Tenkodogo-Yamba batholith that is part of the TTG suite (Naba et al. 2004).

Deposit-scale study suggests the existence of at least three main deformation phases reported as D1_{Ki}, D2_{Ki}, and D3-4_{Ki} (Fontaine et al. 2017). The two first phases (D1_{Ki} and D2_{Ki}) occurred under ductile conditions (P=550-650°C, T=6-8 kbars; Ganne et al. 2012; Fontaine et al. 2017), whereas the others (D3_{Ki}-D4_{Ki}) took place at the ductile-brittle transition (P<4 kbars, T=200-450°C; Fontaine et al. 2017; Ganne et al. 2012; Block et al. 2015). The D1_{Ki} phase corresponds to a relic structural event marked by P1_{Ki} folds, resulting from EW to WNW-ESE compression, which are preserved in low-strain domains between D2_{Ki} shear zones (Fontaine et al. 2017). The S2_{Ki} regional foliation, parallel to the isoclinal P1_{Ki} folding, records a biotite-sillimanite-garnet-amphibole assemblage, suggesting lower to middle amphibolite facies conditions (Fig. 3A).

At the regional scale, the NE-trending D2-related shear zones and the NS-trending MSZ are the main structures controlling the emplacement of the gold mineralization at Kiaka (Fontaine et al. 2017). These structures record dextral-reverse D1 motion and sinistral-reverse D2 reactivation (Tshibubudze et al. 2009; Tshibubudze and Hein 2013). Mineralized envelopes are spatially associated with the NE-trending shear zones and some of them extend along the axial plane of P2_{Ki} isoclinal folds (Fontaine et al. 2017). The sinistral-reverse D2 reactivation is coeval with the emplacement of the Kiaka diorite dated at 2140 ± 7 Ma. The D3-4_{Ki} phases correspond to quartz-carbonate veins that formed during reactivation along D2-related shear zones and retrogression at greenschist facies conditions (Fontaine et al. 2017), likely during or after the ductile-brittle transition.

Tourmaline paragenesis and space-time relationships with gold mineralization

A relative chronology between tectono-metamorphic and hydrothermal events has been proposed by Fontaine et al. (2017), based on crosscutting relationships, hydrothermal

assemblages, and ore mineralogy, identifying two successive stages of gold mineralization and associated hydrothermal alteration in the Kiaka deposit (Fig. 2):

(i) The first main stage corresponds to the early sulfide-rich disseminated gold mineralization related to the D2_{Ki} phase, coeval with emplacement of the biotite-amphibole diorite intrusion (Fig. 2). This mineralization is volumetrically the most important (>80% of the orebodies) and constitutes most of the gold resources with average grades of 1-3 g/t. The ore assemblage consists of 50µm-1mm large anhedral pyrrhotite (60-80%) that is commonly associated with sub-millimetric (200-300 µm) pyrite (10-20%), chalcopyrite (5-10%), arsenopyrite (5-10%), and rare löllingite disseminated in sericitized metagreywacke and partly in metamafic volcanic rocks, containing a biotite-titanite-clinozoisite assemblage. Gold probably occurs as nano-inclusions hosted in, or within, the crystal lattice of pyrite, arsenopyrite, and löllingite. This stage was dated at 2157 ± 24 Ma (Re-Os on pyrrhotite; Le Mignot et al. 2017; Fontaine et al. 2017).

(ii) The second stage is related to formation of a high-grade gold mineralization at 50-60 g/t Au hosted in hydrothermal veins and breccias that formed during the D3_{Ki} to D4_{Ki} phases (Fig. 2). The ore assemblage is composed of pyrrhotite, chalcopyrite, arsenopyrite, electrum, native gold (2-20 µm), and tellurobismuthite, intergrown with clinozoisite, quartz, calcite, and chlorite.

According to Fontaine et al. (2017) and new petrographic observations, two generations of tourmaline are observed in the Kiaka deposit. A first generation of tourmaline (*Tur₁*) is locally found as rounded detrital grains (<10 µm) in quartz-biotite metagreywacke, representing <5% in volume of the host rock. *Tur₁* is also found within garnet-biotite-chlorite-muscovite layers hosted in muscovite schists (Fig. 3A-B), which are affected by the S2_{Ki} foliation and associated folds, suggesting an early formation prior, or during, the D1_{Ki} stage. A second generation of tourmaline (*Tur₂*) is found in the metagreywacke and metamafic volcanic rock (referred

subsequently as metamafic rocks) located close to or within the mineralized zones. This tourmaline is found as large (typically 50-500 μm) zoned porphyroblasts containing sulfide and silicate inclusions. It is locally oriented along the $S_{2\text{Ki}}$ foliation. In the metagreywacke, Tur_2 is intergrown with an assemblage of biotite, clinozoisite, quartz, K-feldspar and disseminated sulfides, including pyrrhotite, chalcopyrite, pyrite, and arsenopyrite (Fig. 3C-D). In the metamafic rock, Tur_2 is intergrown with chlorite (Chl 1, pre- to syn- $D_{1\text{Ki}}$), biotite, titanite, clinozoisite, and pyrrhotite, which are characteristics of the $D_{2\text{Ki}}$ hydrothermal assemblage. Chlorite (Chl 1) inclusions oriented along an early foliation (syn- $D_{1\text{Ki}}$) within the poikiloblastic Tur_2 porphyroblasts (Fig. 5), as well as a chlorite (Chl 2)-biotite assemblage (Fig. 3F), related to the $D_{3\text{Ki}}$ stage and overgrown by Tur_2 , constraint the formation of Tur_2 within syn- to late- $D_{2\text{Ki}}$ event. The assemblage of Chl 1 and biotite is interpreted as a relic from stage $D_{1\text{Ki}}$ that was overprinted by ore stage fluids during the $D_{2\text{Ki}}$ event in replacement zones. In contrast, the assemblage of titanite, clinozoisite, and pyrrhotite is considered to be earlier than $D_{3\text{Ki}}$, because it is cut by chlorite (Chl 3)-calcite veins (Fig. 3E-F). Therefore, the second generation of tourmaline (Tur_2) is interpreted to be of hydrothermal origin and to have formed during the $D_{2\text{Ki}}$ event, coevally with formation of the Kiaka disseminated gold mineralization. In this paper, a specific focus is given on Tur_2 hosted both in metagreywacke and metamafic rocks, in order to determine the fluid sources and processes related to the formation of the first gold event, i.e. the early sulfide-rich disseminated gold mineralization related to the $D_{2\text{Ki}}$ event. Early detrital Tur_1 was not investigated because it formed before the gold mineralization and thus cannot be used as a tracer of ore-forming processes and mineralizing fluids.

SAMPLE DESCRIPTION AND ANALYTICAL METHODS

Sample description

Representative samples of the four main lithologies of the Kiaka deposit were collected from drill cores (spacing >400 m) intersecting the main orebody and alteration zones. Investigation of these lithologies was carried out in order to document the hydrothermal alteration by the gold-bearing fluids and to identify the presence of hydrothermal tourmaline. These lithologies include:

(i) Muscovite schists: they are mostly located in the southern part of the deposit in the footwall of the D2-related shear zone (Fig. 1). They represent 50 to 100 m thick lenses intercalated between metagreywacke and metavolcanic rocks. The muscovite schists contain folded tourmaline (Tur_1)-garnet-biotite-chlorite-muscovite layers (Fig. 3A-B) and rare pyrrhotite grains. The muscovite schist sample (drill KDH75, depth 64.9 m) is located at about 1-2 m from the mineralized zones and is weakly hydrothermally altered.

(ii) Diorite: it consists of sub-vertical intrusive plugs within the metasedimentary sequence in the northern part of the deposit (Fig. 1C). It is interpreted to be contemporaneous with the D2_{Ki} event generating sinistral displacement along mineralized, NE-trending D2 shear zones. The diorite is dominantly composed of plagioclase, amphibole, chlorite, biotite, and quartz. No tourmaline was found in the diorite. Sample KDH337 (depth 44.1m) is located at about 50 m from the mineralized zones and is weakly hydrothermally altered, containing rare grains of pyrrhotite and chalcopyrite associated with titanite.

(iii) Metagreywacke: it is the dominant lithology at Kiaka and forms the southern footwall of a D2-related shear zone hosting the main mineralized zone. Composed of quartz, feldspar, and sillimanite with a granoblastic texture, metagreywacke locally contain disseminated tourmaline grains (Tur_2), about 50 μ m in size (Fig. 3C-D). Sample KDH29 (depth 311.8 m; Fig. 3C-D; Fig. 4) is from a phlogopite-rich alteration zone close to the orebody.

(iv) Metamafic rock: it is intercalated within the metasedimentary sequence forming >50 m thick sequences dipping towards the northwest (Fig. 1). Sample KDH291 (depth 56.2

m; Fig. 3E-F) comes from an alteration zone in proximity to the mineralized envelope. Within this zone, the metamafic rock contains porphyroblasts of hydrothermal tourmaline (*Tur*₂) reaching few millimeters in size, embedded within a chloritized, fine-grained matrix, that locally contains pyrrhotite, titanite and clinozoisite (Fig. 3E).

Scanning electron microscopy

Mineralogical observations of tourmaline were carried out using transmitted-light microscopy and scanning electron microscopy (SEM) at the GeoRessources laboratory (Nancy, France). Tourmaline grains were investigated using a Hitachi S-4800 and a JEOL J7600F scanning electron microscopes, both equipped with SDD-type energy-dispersive X-ray spectrometers (EDS). Backscattered electron (BSE) images were acquired on carbon-coated polished thin sections with an acceleration voltage of 15 kV, adjusting the image contrast to reveal internal zoning within the tourmaline grains. SEM was used to characterize the internal textures of tourmaline and to select representative grains for the *in situ* chemical and isotopic analyses.

Electron probe microanalysis

Major and minor element composition of tourmaline was determined using a Cameca SX100 electron microprobe analyzer (EMPA) equipped with five wavelength-dispersive X-ray spectrometers (WDS) at the GeoRessources laboratory (Nancy, France). Analyses were performed with the following operating conditions: beam current of 20 nA, acceleration voltage of 15 kV, and beam diameter of 1 µm. Counting times on element peaks and backgrounds were 16 sec and 8 sec, respectively, for Si, Al, K, Ca, Fe, Mg, Mn, Ti, and 30 sec and 15 sec, respectively, for Na, Cr, and Cl. The following standards and monochromators were used for the EMPA measurements: albite (Si, Na on TAP), olivine (Mg on TAP), corundum (Al on TAP), orthoclase (K on LPET), andradite (Ca on PET), ilmenite (Ti on LPET, Mn on LIF),

hematite (Fe on LIF), and vanadinite (Cl on LPET). Detection limits are approximately 330 ppm for Si, 300 ppm for Al, 1000 ppm for Fe, 265 ppm for Mg, 250 ppm for Ti, 365 ppm for Mn, 515 ppm for Na, 370 ppm for Ca, 200 ppm for K, and 140 ppm for Cl. Structural formulae of tourmaline were calculated using the WinTcac software (Yavuz et al. 2014) normalizing to 15 cations in Y+Z+T sites and assuming stoichiometric 3 atoms for B and 4 atoms for OH+F, based on the general formula $XY_3Z_6(T_6O_{18})(BO_3)_3V_3W$, where X = Na⁺, Ca²⁺, K⁺, or vacancy site; Y = Fe²⁺, Mg²⁺, Mn²⁺, Al³⁺, Li⁺, Fe³⁺, or Cr³⁺; Z = Al³⁺, Fe³⁺, Ti⁴⁺, Mg²⁺, or Cr³⁺; T = Si⁴⁺, Al³⁺, or B³⁺; V = OH⁻, O²⁻; and W = OH⁻, F⁻, or O²⁻ (Henry et al. 2011). Chemical compositions of tourmaline are reported in weight per cent (wt.%) oxides and the structural formulae are expressed in atoms per formula unit (apfu) (ESM Table 2). X-ray elemental maps were acquired with a 15 kV accelerating voltage, a 100 nA beam current, and a 1 μm^2 electron beam (Fig. 6). The elements Na, Si, Mg, Al, Ca, Ti, and Fe were measured with dwell times of 300 msec each and an acquisition step of 10 μm , for a total map size of 2900 x 3890 μm .

Secondary ion mass spectrometry

Boron isotopic composition of tourmaline was measured by secondary ion mass spectrometry (SIMS) using a Cameca IMS 1280-HR instrument at the CRPG-CNRS (Vandoeuvre-lès-Nancy, France). Analyses were performed on gold-coated polished thin sections that were previously investigated by SEM and EMPA, with a 20 nA beam of primary ions O⁻ accelerated at 13 kV with an ellipsoid ablation spot of 20 μm long axis. The secondary ions ¹⁰B⁺ and ¹¹B⁺ were accelerated at 10 kV and were measured in mono-collection with the axial Faraday cup with a mass resolution power $M/\Delta M = 2000$. Each calculated isotopic ratio ¹¹B/¹⁰B corresponds to 30 cycles of measurement with counting times of 8 sec per cycle on mass 10 and of 4 sec per cycle on mass 11. For each spot, a pre-sputtering of 60 sec was applied immediately before each analysis for surface cleaning. Instrumental mass fractionation (IMF) was determined and

corrected using two tourmaline reference materials corresponding to dravite (Harvard #108796) and schorl (Harvard #112566) described by Dyar et al. (2001) and Leeman and Tonarini (2001). Each standard was measured several times during the analytical SIMS session following a standard-sample bracketing procedure. The summary of the B isotope analyses on the tourmaline reference materials measured by SIMS is reported in ESM Table 1. The matrix effect was corrected using the dravite Harvard #108796 reference material because the tourmaline samples analyzed in this work have dravitic composition. After correction of IMF, the measured $^{11}\text{B}/^{10}\text{B}$ ratios were reported in $\delta^{11}\text{B}$ notation (in ‰) relative to the NIST SRM 951, whose $^{11}\text{B}/^{10}\text{B}$ ratio is 4.04362 (Catanzaro et al. 1970). The external error (2σ) is about 0.13‰ over 28 analyses for the dravite Harvard #108796 and 0.26‰ over 14 analyses for the schorl Harvard #112566. The external error used is that of the dravite Harvard #108796. The total error is the quadratic sum of the internal and external errors and range between 0.2 and 1.2‰ (2σ) on the tourmaline samples with a median value of 0.3‰ (2σ).

Multi-collector – inductively coupled plasma – mass spectrometry

Whole-rock boron content and isotopic compositions of the muscovite schist and diorite were measured using a Thermo Scientific Neptune multi-collector – inductively coupled plasma – mass spectrometer (MC-ICP-MS) at the LhyGeS (Université de Strasbourg-EOST, France). The B extraction procedure was adapted from Lemarchand et al. (2012) and is summarized as follows: 10 mg of powdered sample were mixed with 250 mg of analytical grade K_2CO_3 in a 12 mL PtAu 05 crucible and placed in a muffle furnace at 950°C for 45 min. After cooling, the fusion residue was dissolved in 35 mL of bidistilled HCl 0.2N. Boron was then purified from a 0.5 mL aliquot by a two-step chemical procedure using the cation exchange resin Biorade AG50WX12 and the B-specific resin Amberlite IRA743. The recovered solution was simultaneously analyzed for both B concentration and isotope ratios using the standard-sample-

standard bracketing method. The operational settings for B analyses by MC-ICP-MS are described in details by Roux et al. (2015). Accuracy has been verified by repeated analyses of solution and rock standards (ERM AE120 = − 20.1‰; ERM AE121 = +20.0‰; NRC NASS5 = +39.8‰; GSJ JB2 = +7.2‰). Total B contamination is 15 ng and the analytical uncertainties are 5% and 0.4‰ (2σ) for B concentration and isotope ratios, respectively.

RESULTS

Petrography and textural features of tourmaline

Hydrothermal tourmaline (*Tur*₂) hosted in metagreywacke (sample KDH29-311.8 m; 1.08 g/t Au) ranges in size from 20 to 400 μm with euhedral to sub-euhedral shapes (Fig. 3C-D; Fig. 4). No foliation is clearly preserved in this sample. A metamorphic recrystallization can be observed whereas *Tur*₂ and biotite seem to represent a mineral equilibrium assemblage and to be part of the same hydrothermal D2_{Ki} event. In addition, pyrrhotite and pyrite are characteristic of the assemblage of the low-grade disseminated ore in the Kiaka deposit. The tourmaline grains in the metagreywacke sample occasionally host micro-inclusions of apatite, quartz and pyrrhotite oriented along intra-grain fractures. At microscopic scale, tourmaline has light green to brownish colors in polarized light and is greenish in crossed polarized light. The grains appear homogeneous without core-rim zoning on BSE images (Fig. 4). Nine representative tourmaline grains were selected for *in situ* chemical and isotopic analyses.

Hydrothermal tourmaline (*Tur*₂) hosted in metamafic rock (sample KDH291-56.2 m; 0.05 g/t Au) is characterized by euhedral to sub-euhedral habit and is commonly millimetric in size (Fig. 3E). Under the microscope, poikiloblastic tourmaline porphyroblasts have light yellow to beige colors in polarized light and are yellow-brownish in crossed polarized light. Three representative millimetre-size tourmaline grains intergrown with the biotite-titanite-clinozoisite

D2_{Ki} assemblage were selected for the *in situ* chemical and isotopic analyses (Fig. 5). Those three grains show different crystal orientation relative to the thin section plane, and their internal zoning and compositional variations were investigated in detail. The first tourmaline grain (Grain 1) shows an oblique section relative to the c-axis of about 3 mm wide, the second (Grain 2) shows a transversal section relative to the c-axis of about 9 mm in length, and the third (Grain 3) shows an oblique section relative to the c-axis (Fig. 5). The poikiloblastic tourmaline porphyroblasts host numerous sulfide inclusions (<100 µm up to 0.1 mm in size), including pyrrhotite, chalcopyrite and pyrite, as well as accessory clinozoisite, biotite, amphibole, and chlorite (Chl 2) (Fig. 2). At the grain scale, tourmaline hosted in metamafic rock shows a core-rim zoning on BSE images (Fig. 5C). The core represents the main part of the grains and shows a patchy zoning with dark to medium grey contrasts on BSE images. The rim forms a 100-300 µm thick overgrowth in optical continuity with the core and shows brighter contrasts on BSE images. No dissolution textural evidence between core and rim was observed. X-ray elemental maps show intra-crystalline chemical zoning for Al, Fe, Mg, Ca, and Ti (Fig. 6). The rim is marked by higher Fe contents relative to the core, which is Mg-rich. The intra-grain variation in Ca, Ti, and Al, corresponds to the patchy zoning within the core related to the primary crystal growth of tourmaline.

Chemical composition of tourmaline

Chemical compositions and structural formulae of representative tourmaline grains (*Tur2*) from the Kiaka deposit are reported in the ESM Table 2. Overall, tourmaline compositions show relatively large variations in major elements for FeO (4.65-7.68 wt.%), MgO (7.10-9.52 wt.%), Al₂O₃ (29.59-35.20 wt.%), and relatively small variations in minor elements for Na₂O (1.41-1.70 wt.%), CaO (0.58-2.10 wt.%), MnO (<0.1 wt.%), and TiO₂ (0.19-1.51 wt.%). The

measured K₂O and Cl values are very low (up to 0.14 wt.%), close to or below the EMPA limits of detection.

Tourmaline hosted in the metamafic rock (sample KDH291-56.2 m) belongs to the alkali-group and plots within the compositional field of Al-poor and Fe³⁺-rich metasedimentary rocks in the Al-Fe-Mg diagram (Fig. 7F). Tourmaline has a dravite composition with Mg/(Fe+Mg) = 0.67-0.77 and X_{vacancy}/(X_{vacancy}+Na) = 0.11-0.29 (Fig. 7A). It has moderate contents of Ca (0.10-0.64 apfu), Na (0.50-0.70 apfu), and Al (5.55-6.27 apfu). No correlation is found between the Ca and Ti contents (0.04-0.19 apfu) and the color zoning of tourmaline in polarized light. The core and rim show minor compositional variations that are principally marked by variations of the Fe/Mg ratio, as also seen on X-ray elemental maps (Fig. 6). The chemical variations for tourmaline hosted in the metamafic rock are mostly due to the Mg₊₁Fe₋₁ and □Al₊₁(NaMg)₋₁ exchange vectors, with possible contribution of the (AlO)₊₁(MgOH)₋₁ deprotonation vector (Fig. 7).

Tourmaline hosted in the metagreywacke (sample KDH29-311.8 m) has a distinct chemical composition compared to the metamafic rock-hosted tourmaline. Tourmaline belongs to the alkali-group with a dravite composition and plots into the compositional field of Al-rich metasedimentary rocks in the Al-Fe-Mg diagram (Fig. 7F). It differs mainly from tourmaline hosted in the metamafic rock by lower contents of Ca (0.16-0.22 apfu), Mg (1.75-1.89 apfu), and Na (0.45-0.54 apfu), and by higher contents of X-vacancy (0.25-0.35 apfu), and Al (6.37-6.72 apfu). Tourmaline has dravite composition with Mg/(Fe+Mg) = 0.68-0.73 and X_{vacancy}/(X_{vacancy}+Na) = 0.32-0.44. Variations of tourmaline compositions are mostly explained by the Mg₊₁Fe₋₁ and □Al₊₁(NaMg)₋₁ exchange vectors joining the dravite to foitite endmembers (Fig. 7B-C).

Boron isotope composition of the host rocks and tourmaline

Whole-rock boron isotope analyses were carried out on representative samples of unaltered diorite (sample KDH337-44.1) and muscovite schist (sample KDH75-64.9) collected outside the mineralized envelopes. Boron concentration and isotope analyses yielded reproducible values for each sample (Table 1). The diorite has a B content of 5.6 ppm with an average $\delta^{11}\text{B}$ value of -13.9‰ (n = 2), whereas the muscovite schist contains 71 ppm B and has an average $\delta^{11}\text{B}$ value of -29.2‰ (n = 2). Because the samples are devoid of hydrothermal alteration and the isotopic data are reproducible, the whole-rock boron isotope compositions are considered to be representative of each rock precursor.

In situ boron isotope compositions of tourmaline hosted in the metagreywacke (sample KDH29-311.8 m) and the metamafic rock (sample KDH291-56.2 m) are shown in Fig. 8 and Table 2. The full range of $\delta^{11}\text{B}$ values of tourmaline extends from -25.12‰ to -15.10‰ (n = 49) and overlaps the lower $\delta^{11}\text{B}$ range of tourmaline hosted in orogenic gold deposits worldwide ($\delta^{11}\text{B}$ = -24‰ to +19‰; Fig. 8). Tourmaline hosted in the metamafic rock has heavier boron isotopic composition ($\delta^{11}\text{B}$ = -19.6‰ to -15.1‰; mean = -17.8‰; mode ~ -19.5‰; n = 31) compared to tourmaline hosted in the metagreywacke ($\delta^{11}\text{B}$ = -25.1‰ to -22.0‰; mean = -24.2‰; mode ~ -24.0‰; n = 18). Isotopic analyses of single tourmaline grains reveal $\delta^{11}\text{B}$ variations up to 4.7‰ from core to rim, but show no systematic $\delta^{11}\text{B}$ variation related to sector and patchy zoning. No correlation was found between the chemical and boron isotopic composition of tourmaline.

DISCUSSION

Chemical composition of tourmaline as a monitor of fluid-rock interactions

Tourmaline grains hosted in the metamafic rock and the metagreywacke belong to the dravite series, but they differ by their chemical and boron isotopic compositions. Tourmaline hosted in

the metamafic rock is Al-poor (5.75-6.27 apfu), Fe-rich (0.63-1.05 apfu) and Mg-rich (2.00-2.30 apfu), whereas tourmaline hosted in metagreywacke is Al-rich (6.37-6.72 apfu), Fe-poor (0.65-0.83 apfu) and Mg-poor (1.75-1.89 apfu). This is consistent with the whole-rock contents of Al_2O_3 , Fe_2O_3 and MgO in metamafic rock and metagreywacke, respectively (Table 1; Fontaine et al. 2017), which suggests a host rock control on the chemical composition of tourmaline (except for boron), as proposed by other studies (e.g. van Hinsberg et al. 2011; Hazarika et al. 2015; 2016; Kalliomäki et al. 2017; Harlaux et al. 2019). In addition, metamafic rock-hosted tourmaline has lower X-vacancy contents (0.08-0.24 apfu) and higher Na+Ca contents (0.76-0.92 apfu), whereas metagreywacke-hosted tourmaline has higher X-vacancy contents (0.25-0.35 apfu) and lower Na+Ca contents (0.65-0.75 apfu). This is also consistent with the higher whole-rock contents of CaO , Na_2O and K_2O in the metamafic rock compared to metagreywacke (Table 1; Fontaine et al. 2017). In the X-vacancy vs. Al total and Fe vs. Al diagrams (Fig. 7C, D), metamafic rock-hosted tourmaline shows large Al variations (5.75-6.27 apfu) reflecting the $(\text{AlO})_{+1}(\text{MgOH})_{-1}$ deprotonation exchange vector, whereas metagreywacke tourmaline has higher Al and X-vacancy contents projecting along the $\square\text{Al}_{+1}(\text{NaMg})_{-1}$ exchange vector.

These variations may reflect variable degrees of interaction between the hydrothermal fluid and the host rocks. For comparison, syn-ore hydrothermal tourmaline from orogenic gold deposits in the Loulo Gold District in Mali (Lambert-Smith et al. 2016) shows large variations of the $\text{Mg}/(\text{Fe}+\text{Mg})$ ratio (0.27-0.96) and have lower Ca contents (0.01-0.09 apfu) and higher Na contents (0.62-0.89) compared to hydrothermal tourmaline from Kiaka (Fig. 7). The composition of the X-site in tourmaline is dominantly controlled by the Na and Ca concentrations in the coexisting aqueous fluid, being therefore a function of the fluid salinity (von Goerne et al. 2001, 2011; Dutrow and Henry 2016, 2018). The relative high contents of Na (0.45-0.70 apfu, average = 0.61 apfu) and Ca (0.10-0.37 apfu, average = 0.24 apfu) and the

relative low contents of X-vacancy (0.08-0.35 apfu, average = 0.15 apfu) in hydrothermal tourmaline (*Tur*₂) suggest that the fluid was of low to moderate salinity. The tourmaline-bearing ore assemblage is interpreted to have formed during the D2_{Ki} stage at temperatures of 371-413°C based on chlorite (Chl 2) thermometry (Fontaine et al. 2017). Additionally, arsenopyrite in contact with pyrrhotite and löllingite in quartz-biotite metagreywacke contains 35.4-36.5 atm% of As, yielding temperatures of 360-475°C (Fontaine et al. 2017). Assuming a median temperature of 400°C and an average Na = 0.6 apfu in tourmaline, a salinity of ca. 3 wt.% NaCl equiv can be estimated for the fluid in equilibrium with the assemblage tourmaline + quartz + chlorite (von Goerne et al. 2001). Tourmaline precipitation from hydrothermal fluids requires acidic to near-neutral conditions (pH <6) that favor the formation of stable trigonal complexes [B(OH)₃] in the fluid (Morgan and London 1989; Henry and Dutrow 1996). The development of pervasive sericitization associated with disseminated tourmaline and clinozoisite in the metagreywacke (Fontaine et al. 2017) suggests that the fluid was moderately acidic. The composition of tourmaline from Kiaka is dominantly controlled by the Fe²⁺₊₁Mg²⁺₋₁ and □Al₊₁(NaMg)₋₁ exchange vectors with no contribution of the Fe³⁺₊₁Al³⁺₋₁ homovalent substitution (Fig. 7), which suggests low Fe³⁺/Fe²⁺ ratios and reduced fluid conditions. These arguments suggest that hydrothermal tourmaline (*Tur*₂) likely formed from moderately high temperature (ca. 400°C), moderately acidic, reduced, and low-salinity hydrothermal fluids and that its chemical composition (except for B, Na and Ca) was buffered by the host rock during fluid-rock interactions.

Origin of fluids and boron for formation of the Kiaka gold deposit

The source of boron and mineralizing fluids at Kiaka can be discussed in terms of proximal vs. distal, as well as magmatic vs metamorphic origin. In the metagreywacke and the metamafic rock, the boron budget is largely dominated by hydrothermal tourmaline (*Tur*₂), which is the

493 main boron-bearing mineral in those rocks. Considering that basalts have typically very low
 494 boron contents (Table 1; <0.1 to 5 ppm; Leeman and Sisson 1996; Marschall 2018), it is
 495 unlikely that the boron required to form *Tur*₂ in the metamafic rock was derived from the
 496 basaltic precursor. The metagreywacke contains two generations of tourmaline: one generation
 497 is detrital (*Tur*₁), being part of the mineral assemblage of the protolith, whereas the other one is
 498 hydrothermal (*Tur*₂), being formed during the D2_{Ki} event. As detrital *Tur*₁ remained stable in
 499 the metagreywacke during the prograde and retrograde metamorphism, it seems unlikely that
 500 *Tur*₁ was a viable source of boron for formation of *Tur*₂, even if we cannot definitively exclude
 501 the potential destabilization of *Tur*₁ in deep-seated metagreywacke lithologies.

502 We may also exclude the diorite as a proximal boron source because of its low boron content
 503 (B = 5.6 ppm, Table 1) and its absence of significant hydrothermal alteration, arguing against
 504 the release of boron-rich magmatic fluids or post-magmatic hydrothermal alteration. Another
 505 possible candidate could be the younger unfoliated biotite granites that have intruded the TTG
 506 basement between ca. 2120 Ma and 2100 Ma (Vegas et al. 2008; Baratoux et al. 2011). These
 507 granitic rocks emplaced through transcurrent shearing along the Manga Fada N’Gourma
 508 greenstone belt and the related amphibolite-facies metamorphism attributed to contact
 509 metamorphism (Naba et al. 2004; Vegas et al. 2008) has been dated at 2105 ± 30 Ma (Pb-Pb on
 510 zircon; Castaing et al. 2003). However, none of these granitic rocks has been described in the
 511 district of Kiaka and no granite intercept was found in the investigated drill cores.

512 A proximal origin of boron-rich fluids may therefore be discarded. The boron isotope
 513 compositions of hydrothermal tourmaline (*Tur*₂) from Kiaka ($\delta^{11}\text{B} = -25.1\text{‰}$ to -15.1‰ ; Fig.
 514 8) fall outside the typical $\delta^{11}\text{B}$ range for tourmaline hosted in granitic rocks (-15‰ to $+5\text{‰}$;
 515 Marschall and Jiang 2011; Trumbull and Slack 2018), although they partly overlap with the
 516 $\delta^{11}\text{B}$ range of tourmaline from granite-related veins (-22‰ to -3‰ ; Fig. 8).

517 A magmatic-hydrothermal origin of the fluid can be excluded, because (i) no contemporaneous
 518 granitic intrusion is found nearby the Kiaka deposit, (ii) age constraints exclude the diorite plug
 519 as a magmatic source of boron, and, to a lesser extent, (iii) the mineralization is hosted in thick
 520 metasedimentary-metavolcanic units. A meta-evaporitic fluid origin ($\delta^{11}\text{B} = +5\text{‰}$ to $> +30\text{‰}$)
 521 can also be ruled out. In contrast, the B isotope values of *Tur*₂ are compatible with those of
 522 tourmaline hosted in metasedimentary rocks ($\delta^{11}\text{B} = -26\text{‰}$ to $+1\text{‰}$; Nakano and Nakamura
 523 2001; Bebout and Nakamura 2003; Marschall and Jiang 2011; Berryman et al. 2017; Fig. 8).
 524 Despite the general diachronism observed from east to west in the southern WAC (Parra-Avila
 525 et al. 2017), comparison with the Loulo Mining District in Mali is of interest. Lambert-Smith
 526 et al. (2016) have used geochemistry and boron isotopy of tourmaline to discriminate fluid
 527 source regions. The $\delta^{11}\text{B}$ values in syn-ore tourmaline indicate a dominant fluid contribution
 528 from clastic metasediments and carbonate rocks, suggesting metamorphic devolatilization in
 529 the host terrane as the most likely process that produced the ore-forming fluids. It seems likely
 530 for the Kiaka deposit that hydrothermal tourmaline crystallized from a boron-rich metamorphic
 531 fluid, of distal origin, derived from deep-seated metasediments.

532 Boron isotope compositions of tourmaline hosted in the metamafic rock ($\delta^{11}\text{B} = -19.6\text{‰}$ to -
 533 15.1‰) and the metagreywacke ($\delta^{11}\text{B} = -25.1\text{‰}$ to -22.0‰) show a significant difference of
 534 $\delta^{11}\text{B}$ values (up to 10‰), which suggests variable degrees of interactions between the boron-
 535 rich hydrothermal fluid and the host rocks, as also supported by the chemical compositions of
 536 tourmaline. The muscovite schists may represent a potential source for the boron-rich fluids
 537 because they have a relatively high B content (71 ppm, Table 1), which is commonly associated
 538 with micas (Leeman and Sisson 1996; Nakano and Nakamura 2001; Trumbull and Slack 2018).
 539 Muscovite breakdown reactions in metapelitic rocks at $P \leq 4$ kbar and $T \leq 650^\circ\text{C}$ (Thompson
 540 1982; Vielzeuf and Holloway 1988; Spear et al. 1999) can produce a low-salinity, reduced, and
 541 boron-rich metamorphic fluid (Moran et al. 1992; Henry and Dutrow 1996; Nakano and

542 Nakamura 2001; Kawakami and Ikeda 2003). In order to evaluate whether hydrothermal
 543 tourmaline could have formed from boron-rich fluids derived from devolatilization of
 544 muscovite schists at depth, we calculated the tourmaline-fluid B isotope fractionation according
 545 to the Rayleigh fractionation model of Marschall et al. (2009) and using the fractionation factors
 546 of Meyer et al. (2008). Considering a temperature of 650°C for the muscovite breakdown
 547 reaction, an average $\delta^{11}\text{B} = -29.2\text{‰}$ for the muscovite schist (Table 1), and a muscovite-fluid
 548 boron isotopic fractionation of -7.7‰ (Wunder et al. 2005), we estimated a $\delta^{11}\text{B} = -21.5\text{‰}$ for
 549 the expelled metamorphic fluid. At 650°C, the minimum boron content of this fluid would be
 550 about 1.0 to 2.5 wt.% B_2O_3 (London 2011). The evolution of the B isotopic composition of this
 551 fluid during its ascent through metamorphic rocks at amphibolite facies conditions was
 552 calculated using the fractionation for a stepwise decreasing temperature from 650 to 350°C
 553 following the model of Büttner et al. (2016). Considering an initial fluid composition of $\delta^{11}\text{B} =$
 554 -21.5‰ at 650°C, progressive fractionation by removing 60 to 90% of boron from the fluid (F
 555 $= 0.1\text{--}0.4$) results in a shift towards higher $\delta^{11}\text{B}$ values of -19.6‰ to -14.9‰ (Fig. 9).
 556 Tourmaline precipitating from this fluid would acquire $\delta^{11}\text{B}$ compositions comprised between
 557 -20‰ and -18‰ . At 400°C, a representative temperature for Tur_2 formation at Kiaka, the fluid
 558 would have a $\delta^{11}\text{B} = -16.3\text{‰}$ and the corresponding tourmaline would acquire a $\delta^{11}\text{B} = -19.1\text{‰}$
 559 (Fig. 7). These $\delta^{11}\text{B}$ values fall into the range of $\delta^{11}\text{B} = -25.1\text{‰}$ to -15.1‰ (average $= -20.1\text{‰}$)
 560 measured for hydrothermal tourmaline from Kiaka. The differences of $\delta^{11}\text{B}$ values between
 561 tourmaline hosted in the metagreywacke (average $= -24.2\text{‰}$) and the metamafic rock (average
 562 $= -17.8\text{‰}$) are interpreted to reflect variable degrees of interactions, at constant temperature
 563 (ca. 400°C), between the host rocks of initially distinct isotopic compositions and the boron-
 564 rich metamorphic fluid.

565 In summary, hydrothermal tourmaline (Tur_2) from Kiaka formed through moderately high-
 566 temperature fluid-rock interactions between boron-rich metamorphic fluids and the country

rocks, resulting in the local uptake of Al, Fe, and Mg required for tourmaline formation. We propose that the source of the boron-rich fluids was derived from muscovite schists similar to those exposed at Kiaka but located at a deeper level in the metamorphic nappe. The present results indicate that neither proximal country rocks of the Kiaka deposit nor ascending granitic magmas could be viable sources of fluids and boron. However, the isotopic data are consistent with fluids and boron being issued from devolatilization of deep-seated muscovite schists during the D2_{Ki} event, which relates to the prograde-to-peak amphibolite facies regional metamorphism. This interpretation is supported by mineral-equilibria modelling suggesting that exhumation of metasediments can produce important amounts of metamorphic fluids at temperatures near 500°C (Vry et al. 2010).

CONCLUSIONS

In the Kiaka orogenic gold deposit, hydrothermal tourmaline (*Tur*₂) is commonly associated with the proximal alteration assemblage in the host rocks. Mineralogical observations suggest that deposition of *Tur*₂ was synchronous with the early sulfide-rich disseminated gold mineralization coeval with the D2_{Ki} phase, corresponding to the regional prograde-to-peak metamorphism. Hydrothermal tourmaline hosted in metamafic rock and metagreywacke has a dravite composition, but shows variable major element contents, mainly in Al, Mg, and Fe, thus suggesting a host rock buffering. Boron isotope compositions of tourmaline range between -25.1‰ and -15.1‰, with differences between tourmaline hosted in the metamafic rock ($\delta^{11}\text{B} = -19.6\text{‰}$ to -15.1‰) and tourmaline hosted in the metagreywacke ($\delta^{11}\text{B} = -25.1\text{‰}$ to -22.0‰). Modeling of tourmaline-fluid boron isotope fractionation argue for a metamorphic origin of the mineralizing fluids that were produced during devolatilization of deep-seated muscovite schists. We propose that hydrothermal tourmaline (*Tur*₂) and the synchronous disseminated gold mineralization resulted from moderately high-temperature (ca. 400°C) interactions between a

boron-rich hydrothermal fluid and the metamorphic host rocks at recorded amphibolite facies conditions.

Acknowledgments

We are grateful to AMIRA International and industry sponsors, including AusAid and the ARC Linkage Project LP110100667, for their support on the WAXI project (P934A). This study is part of the WAXI 2 program (<http://waxi2.org/>). We also thank Drs. James Lambert-Smith and Crystal LaFlamme for their constructive and thorough reviews that greatly helped improving the quality of the original manuscript. Finally, we thank the Editor-in-Chief Dr. Georges Beaudoin and the Guest Editor Dr. Nicolas Thébaud for their comments and the editorial handling.

References

- Abouchami W, Boher M, Michard A, Albarede F (1990) A major 2.1 Ga event of mafic magmatism in west Africa: An Early stage of crustal accretion. *J Geophys Res Solid Earth* 95:17605-17629
- Allibone A, Hayden P, Cameron G, Duku F (2004) Paleoproterozoic Gold Deposits Hosted by Albite- and Carbonate-Altered Tonalite in the Chirano District, Ghana, West Africa. *Econ Geol* 99:479-497
- Anglin CD, Jonasson IR, Franklin JM (1996) Sm-Nd dating of scheelite and tourmaline; implications for the genesis of Archean gold deposits, Val d'Or, Canada. *Econ Geol* 91:1372-1382
- Augustin J, Gaboury D, (2017) Paleoproterozoic plume-related basaltic rocks in the Mana gold district in western Burkina Faso, West Africa: Implications for exploration and the source of gold in orogenic deposits. *J Afr Sci* 129:17-30
- Augustin J, Gaboury D, Crevier M (2017) Structural and gold mineralizing evolution of the world-class orogenic Mana district, Burkina Faso: Multiple mineralizing events over 150 million years. *Ore Geo Rev* 91:981-1012
- Baksheev, IA, Prokofiev VY, Trumbull RB, Wiedenbeck M, Yapaskurt VO (2015) Geochemical evolution of tourmaline in the Darasun gold district, Transbaikial region, Russia: evidence from chemical and boron isotopic compositions. *Miner Deposita* 50:125-138
- Baratoux L, Metelka V, Naba S, Jessel MW, Gregoire M, Ganne J (2011) Juvenile Paleoproterozoic crust evolution during the Eburnean orogeny (2.2-2.0 Ga), western Burkina Faso. *Precambrian Res* 191:18-45

626 Beaudoin G, Rollion-Bard C, Giuliani G (2013) The boron isotope composition of tourmaline
627 from the Val-d'Or orogenic gold deposits, Québec, Canada. 12th SGA Biennial Meeting:
628 Mineral deposit research for a high-tech world 3:1090-1092

629 Bebout GE, Nakamura E (2003) Record in metamorphic tourmalines of subduction-zone
630 devolatilization and boron cycling. *Geology* 31:407-410

631 Berryman EJ, Kutzschbach M, Trumbull RB, Meixner A, van Hinsberg V, Kasemann SA,
632 Franz G (2017) Tourmaline as a petrogenetic indicator in the Pfitsch Formation, Western
633 Tauern Window, Eastern Alps. *Lithos* 284:138-155

634 Béziat D, Bourges F, Debat P, Fuchs Y, Lompo M, Martin F, Kiema S, Tollon F (1999) The
635 Guibaré and Fété Kolé gold-bearing tourmaline-quartz veins in the Birimian greenstone
636 belt of Burkina Faso. *Can Mineral* 37:575-591

637 Béziat D, Dubois M, Debat P, Nikiéma S, Salvi S, Tollon F (2008) Gold metallogeny in the
638 birimian craton of Burkina Faso (West Africa). *J Afr Earth Sci* 50:215-233

639 Block S, Ganne J, Baratoux L, Zeh A, Parra-Avila A, Jessel M, Ailleres L, Siebenaller L (2015)
640 Petrological and geochronological constraints on lower crust exhumation during
641 Paleoproterozoic (Eburnean) orogeny, NW Ghana, West African Craton, *Journal of*
642 *Metamorphic Geology* 33:463-494

643 Block S, Baratoux L, Zeh A, Laurent O, Bruguier P, Jessel M, Ailleres L, Sagna R, Parra-Avila
644 LA, Bosch D (2016) Paleoproterozoic juvenile crust formation and stabilisation in the
645 south-eastern West African Craton (Ghana); New insights from U-Pb-Hf zircon data and
646 geochemistry. *Precambrian Res* 287:1-30

647 Boher M, Abouchami W, Michard A, Albarede F, Arndt NT (1992) Crustal growth in West
648 Africa at 2.1 Ga. *J Geophys Res Solid Earth* 97:345-369

649 Burrows D, Spooner E (1987) Generation of magmatic H₂O-CO₂ fluid enriched in Mo, Au and
650 W within an Archean sodic granodiorite stock, Mink Lake, North Western Ontario. Econ
651 Geol 82:1931–1957

652 Büttner SH, Reid W, Glodny J, Wiedenbeck M, Chuwa G, Moloto T, Gucsik A (2016) Fluid
653 sources in the Twangiza–Namoya Gold Belt (Democratic Republic of Congo): Evidence
654 from tourmaline and fluid compositions, and from boron and Rb–Sr isotope systematics.
655 Precambrian Res 280:161-178

656 Byerly GR, Palmer MR (1991) Tourmaline mineralization in the Barberton greenstone belt,
657 South Africa: early Archean metasomatism by evaporite-derived boron. Contrib Mineral
658 Petr 107:387-402

659 Castaing C, Bila M, Milési JP, Thiéblemont D, Le Metour J, Egal E, Zunimo C (2003) Notice
660 explicative de la carte géologique et minière du Burkina Faso à 1/1 000 000 (3^{ème} ed)

661 Catanzaro E, Champion C, Garner E, Marinenko G, Sappenfield K, Shields W (1970) Boric
662 acid: isotopic and assay standard reference materials. National Bureau of Standards (US)
663 Special Publications 260-17:1-71

664 Davis J, Miller J, Thébaud N, McCuaig C, Begg G, Jessell M, Hein K, Baratoux L (2015)
665 Craton-scale lithostratigraphic correlation as an insight for the geodynamic evolution of
666 the southern West African Craton. Proceeding of the 13th Biennial SGA Meeting 4:1587-
667 1590

668 Dutrow BL, Henry DJ (2011) Tourmaline: a geologic DVD. Elements 7:301-306

669 Dutrow BL, Henry DJ (2016) Fibrous tourmaline: a sensitive probe of fluid compositions and
670 petrologic environments. Can Mineral 54:311-335

671 Dutrow BL, Henry DJ (2018) Tourmaline compositions and textures: reflections of the fluid
672 phase. J Geosci 63:99-110

673 Dyar MD, Wiedenbeck M, Robertson D, Cross LR, Delaney JS, Ferguson K, Francis CA, Grew
674 ES, Guidotti CV, Hervig RL, Hughes JM, Husler J, Leeman W, McGuire AV, Rhede D,
675 Rothe H, Paul RL, Richards I, Yates M (2001) Reference minerals for the microanalysis
676 of light elements. *Geostand Newslett* 25:441-463

677 Egal E, Thiéblemont D, Lahondère D, Guerrot C, Costea CA, Iliescu D, Delor C, Goujou JC,
678 Lafon JM, Tegye M (2002) Late Eburnean granitization and tectonics along the western
679 and northwestern margin of the Archean Kénéma–Man domain (Guinea, West African
680 Craton). *Precambrian Res* 117:57-84

681 Eglinger A, Thébaud N, Zeh A, Davis J, Miller J, Parra-Avila LA, Loucks R, McCuaig C,
682 Belousova E (2017) New insights into the crustal growth of the Paleoproterozoic margin
683 of the Archean Kéména-Man domain, West African craton (Guinea): Implications for
684 gold mineral system. *Precambrian Res* 292:258-289

685 Feybesse JL, Milési JP (1994) The Archaean/Proterozoic contact zone in West Africa: a
686 mountain belt of décollement thrusting and folding on a continental margin related to 2.1
687 Ga convergence of Archaean cratons? *Precambrian Res* 69:199-227

688 Feybesse JL, Billa M, Guerrot C, Duguey E, Lescuyer JL, Milési JP, Bouchot V (2006) The
689 paleoproterozoic Ghanaian province: Geodynamic model and ore controls, including
690 regional stress modeling. *Precambrian Res* 149:149-196

691 Fontaine A, Eglinger A, Ada K, André-Mayer AS, Reisberg L, Siebenaller L, Le Mignot E,
692 Ganne J, Poujol M (2017) Geology of the world-class Kiaka polyphase gold deposit, West
693 African Craton, Burkina Faso. *J Afr Earth Sci* 126:96-122

694 Fougere D, Micklethwaite S, Ulrich S, Miller J, Godel B, Adams DT, McCuaig TC (2017)
695 Evidence for two stages of mineralization in West Africa's largest gold deposit: Obuasi,
696 Ghana. *Econ Geology* 112:3-22

697 Frei R, Pettke T (1996) Mono-sample Pb-Pb dating of pyrrhotite and tourmaline: Proterozoic
 698 vs. Archean intracratonic gold mineralization in Zimbabwe. *Geology* 24:823-826
 699 Fusswinkel T, Wagner T, Sakellaris G (2017) Fluid evolution of the Neoproterozoic Pampalo
 700 orogenic gold deposit (E Finland): Constraints from LA-ICPMS fluid inclusion
 701 microanalysis. *Chem Geol* 450:96-121
 702 Ganne J, De Andrade V, Weinberg RF, Vidal O, Dubacq B, Kagambega N, Naba S, Baratoux
 703 L, Jessell M, Allibon J (2012) Modern-style plate subduction preserved in the
 704 Palaeoproterozoic West African craton. *Nat Geosci* 5:60-65
 705 Goldfarb R, Baker T, Dubé B, Groves DI, Hart CJR, Gosselin P (2005) Distribution, character
 706 and genesis of gold deposits in metamorphic terranes. In: Hedenquist JW, Thompson
 707 JFH, Goldfarb RG, Richards JP (eds) *Economic geology 100th Anniversary volume*, Soc
 708 Econ Geol, Littleton, Colorado, USA, pp 407-450
 709 Goldfarb RJ, Groves DI (2015) Orogenic gold: Common or evolving fluid and metal sources
 710 through time. *Lithos* 233:2-26
 711 Goldfarb RJ, André-Mayer AS, Jowitt SM, Mudd GM (2017) West Africa: The World's
 712 Premier Paleoproterozoic Gold Province. *Econ Geol* 112:123-143
 713 Grenholm M, Jessell M, Thébaud N (2019) Paleoproterozoic volcano-sedimentary series in the
 714 ca. 2.27–1.96 Ga Birimian Orogen of the southeastern West African Craton. *Precambrian*
 715 *Res* 328:161-192
 716 Groves DI, Santosh M, Deng J, Wang Q, Yang L, Zhang L (2019) A holistic model for the
 717 origin of orogenic gold deposits and its implications for exploration. *Miner Deposita*
 718 55:275-292
 719 Harlaux M, Mercadier J, Marignac C, Villeneuve J, Mouthier B, Cuney M (2019) Origin of the
 720 atypical Puy-les-Vignes W breccia pipe (Massif Central, France) constrained by trace
 721 element and boron isotopic composition of tourmaline. *Ore Geol Rev* 114:103132

722 Hazarika P, Mishra B, Pruseth KL (2015) Diverse Tourmaline Compositions from Orogenic
 723 Gold Deposits in the Hutti-Maski Greenstone Belt, India: Implications for Sources of
 724 Ore-Forming Fluids. *Econ Geol* 110:337-353
 725 Hazarika P, Mishra B, Pruseth KL (2016) Scheelite, apatite, calcite and tourmaline
 726 compositions from the late Archean Hutti orogenic gold deposit: Implications for
 727 analogous two stage ore fluids. *Ore Geol Rev* 72:989-1003
 728 Henry DJ, Guidotti CV (1985) Tourmaline as a petrogenetic indicator mineral: an example from
 729 the staurolite-grade metapelite of NW Maine. *Am Mineral* 70:1-15
 730 Henry DJ, Dutrow BL (1996) Metamorphic tourmaline and its petrologic applications. In: Grew
 731 ES, Anovitz LM (eds) *Boron, Mineralogy, Petrology and Geochemistry*. *Rev Mineral*
 732 33:503-557
 733 Henry DJ, Novak M, Hawthorne FC, Ertl A, Dutrow BL, Uher P, Pezzotta F (2011)
 734 Nomenclature of the tourmaline-supergroup minerals. *Am Mineral* 96:895-913
 735 Hottin g, Ouédraogo OF (1976) Carte géologique de la République de Haute-Volta. Direction
 736 de la Géologie et des Mines Ouagadougou 58p
 737 Jiang SY (1998) Stable and radiogenic isotope studies of tourmaline: an overview. *J Czech*
 738 *Geol Soc* 43:1-2
 739 Jiang SY, Palmer MR, Yeats CJ (2002) Chemical and boron isotopic compositions of
 740 tourmaline from the Archean Big Bell and Mount Gibson gold deposits, Murchison
 741 Province, Yilgarn Craton, Western Australia. *Chem Geol* 188:229-247
 742 Kalliomäki H, Wagner T, Fusswinkel T, Sakellaris G (2017) Major and trace element
 743 geochemistry of tourmalines from Archean orogenic gold deposits: Proxies for the origin
 744 of gold mineralizing fluids? *Ore Geol Rev* 91:906-927

745 Kawakami T, Ikeda T (2003) Boron in metapelites controlled by the breakdown of tourmaline
 746 and retrograde formation of borosilicates in the Yanai area, Ryoke metamorphic belt, SW
 747 Japan. *Contrib Mineral Petr* 145:131-150
 748 King RW, Kerrich RW (1989) Strontium isotope compositions of tourmaline from lode gold
 749 deposits of the Archean Abitibi Greenstone belt (Ontario-Quebec, Canada): Implications
 750 for source reservoirs. *Chem Geol* 79:225-240
 751 Kotzer TG, Kyser TK, King RW, Kerrich R (1993) An empirical oxygen- and hydrogen-isotope
 752 geothermometer for quartz-tourmaline and tourmaline-water. *Geochim Cosmochim Ac*
 753 57:3421-3426
 754 Krienitz MS, Trumbull R, Hellmann A, Kolb J, Meyer F, Wiedenbeck M (2008) Hydrothermal
 755 gold mineralization at the Hira Buddini gold mine, India: constraints on fluid evolution
 756 and fluid sources from boron isotopic compositions of tourmaline. *Miner Deposita*
 757 43:421-434
 758 Labou I, Benoit M, Baratoux L, Grégoire M, Ndiaye PM, Thebaud N, Béziat D, Debat P (2020)
 759 Petrological and geochemical study of Birimian ultramafic rocks within the West African
 760 Craton: Insights from Mako (Senegal) and Loraboué (Burkina Faso)
 761 Iherzolite/harzburgite/wehrlite associations. *J Afr Earth Sci* 162:103677
 762 Lambert-Smith JS, Rocholl A, Treloar PJ, Lawrence DM (2016) Discriminating fluid source regions in
 763 orogenic gold deposits using B-isotopes. *Geochim Cosmochim Ac* 194:57-76
 764 Le Mignot E, Reisberg L, André-Mayer AS, Bourassa Y, Fontaine A, Miller J (2017) Re-Os
 765 Geochronological Evidence for Multiple Paleoproterozoic Gold Events at the Scale of the
 766 West African Craton. *Econ Geol* 112:145-168
 767 Leeman W P, Sisson VB (1996) Geochemistry of boron and its implications for crustal and
 768 mantle processes. In: Grew ES, Anovitz LM (eds) *Boron, Mineralogy, Petrology and*
 769 *Geochemistry*. *Rev Mineral* 33:645-707

770 Leeman WP, Tonarini S (2001) Boron isotopic analysis of proposed borosilicate mineral
 771 reference samples. *Geostand Newslett* 25:399-403
 772 Lemarchand D, Cividini D, Turpault MP, Chabaux F (2012) Boron isotopes in different grain
 773 size fractions: Exploring past and present water-rock interactions from two soil profiles
 774 (Strengbach, Vosges Mountains). *Geochim Cosmochim Acta* 98:78-93
 775 London D (2011) Experimental synthesis and stability of tourmaline: a historical overview. *Can*
 776 *Mineral* 49:117-136
 777 Markwitz V, Hein KAA, Miller J (2016) Compilation of West African mineral deposits: spatial
 778 distribution and mineral endowment. *Precambrian Res* 274:61-81
 779 Marschall HR (2018) Boron isotopes in the ocean floor realm and the mantle. In Marschall H,
 780 Foster G (eds) *Boron Isotopes: The Fifth Element. Advances in Isotope Geochemistry*,
 781 Springer-Verlag, pp 189-215
 782 Marschall HR, Jiang SY (2011) Tourmaline Isotopes: No Element Left Behind. *Elements*
 783 7:313-319
 784 Marschall HR, Meyer C, Wunder B, Ludwig T, Heinrich W (2009) Experimental boron isotope
 785 fractionation between tourmaline and fluid: confirmation from in situ analyses by
 786 secondary ion mass spectrometry and from Rayleigh fractionation modelling. *Contrib*
 787 *Miner Petrol* 158:675–681
 788 Masurel Q, Thébaud N, Miller J, Ulrich S, Hein KAA, Cameron G, Béziat D, Bruguier O, Davis
 789 JA (2017) Sadiola Hill: A World-Class Carbonate-Hosted Gold Deposit in Mali, West
 790 Africa. *Econ Geol* 112:23-47
 791 Masurel Q, Eglinger A, Thébaud N, Allibone A, André-Mayer AS, McFarlane H, Miller J,
 792 Jessell M, Aillères L, Vanderhaeghe O, Salvi S, Baratoux L, Perrouy S, Begg G,
 793 Fougereuse D, Hayman P, Ousmane W, Tshibubudze A, Parra-Avila L, Kouamelan A,
 794 Ofori P (submitted) Gold metallogeny of the Paleoproterozoic part of the southern

795 West African Craton: capturing distinct pulses within a Paleoproterozoic orogenic cycle.
 796 Miner Deposita

797 McFarlane HB, Ailleres L, Betts P, Ganne J, Baratoux L, Jessel MW, Block S (2019) Episodic
 798 collisional orogenesis and lower crust exhumation during the Palaeoproterozoic Eburnean
 799 Orogeny: Evidence from the Sefwi Greenstone Belt, West African Craton. *Precambrian*
 800 *Res*: 325:88-110

801 McFarlane CRM, Mavrogenes J, Lentz D, King K, Allibone A, Holcombe R (2011) *Geology*
 802 and Intrusion-Related Affinity of the Morila Gold Mine, Southeast Mali. *Econ Geol*
 803 106(5):727-750

804 Meyer C, Wunder B, Meixner A, Romer RL, Heinrich W (2008) Boron-isotope fractionation
 805 between tourmaline and fluid: an experimental re-investigation. *Contrib Mineral Petr*
 806 156:259-267

807 Milesi JP, Feybesse JL, Pinna P, Deschamps Y, Kampunzu H, Muhongo S, Lescuyer JL, Le
 808 Goff E, Delor C, Billa M, Ralay F, Henry C (2004) Geological map of Africa
 809 1:10,000,000. SIGAfrique project. In: 20th Conference of African Geology. BRGM,
 810 Orléans, France, 2-7 June

811 Molnár F, Mänttari I, O'Brien H, Lahaye Y, Pakkanen L, Johanson B, Käpyaho A, Sorjonen-
 812 Ward P, Whitehouse M, Sakellaris G (2016) Boron, sulphur and copper isotope
 813 systematics in the orogenic gold deposits of the Archaean Hattu schist belt, eastern
 814 Finland. *Ore Geol Rev* 77:133-162

815 Moran AE, Sisson VB, Leeman WP (1992) Boron depletion during progressive metamorphism:
 816 implications for subduction processes. *Earth Planet Sc Lett* 111:331–349

817 Morgan GB, London D (1989) Experimental reactions of amphibolite with boron-bearing
 818 aqueous fluids at 200 Mpa: implications for tourmaline stability and partial melting in
 819 mafic rocks. *Contrib Mineral Petr* 102:281-297

820 Mueller AG, de Laeter JR, Groves DI (1991) Strontium isotope systematics of hydrothermal
821 minerals from epigenetic Archean gold deposits in the Yilgarn Block, Western Australia.
822 Econ Geol 86:780-809

823 Naba S, Lompo M, Debat P, Bouchez JL, Béziat D (2004) Structure and emplacement model
824 for late-orogenic Paleoproterozoic granitoids: the Tenkodogo-Yamba elongate pluton
825 (Eastern Burkina Faso). J Afr Earth Sci 38:41-57

826 Nakano T, Nakamura E (2001) Boron isotope geochemistry of metasedimentary rocks and
827 tourmalines in a subduction zone metamorphic suite. Phy Earth Planet In 127:233-252

828 Parra-Avila LA, Kemp AIS, Fiorentini ML, Belousova E, Baratoux L, Block S, Jessell M,
829 Bruguier O, Begg GC, Miller J, Davis J, McCuaig TC (2017) The geochronological
830 evolution of the Paleoproterozoic Baoulé-Mossi domain of the Southern West African
831 Craton. Precambrian Res 300:1-27

832 Parra-Avila LA, Baratoux L, Eglinger A, Fiorentini ML, Block S (2019) The Eburnean
833 magmatic evolution across the Baoulé-Mossi domain: Geodynamic implications for the
834 West African Craton. Precambrian Res 332 [105392]

835 Perrouty S, Aillères L, Jessell MW, Baratoux L, Bourassa Y, Crawford B (2012) Revised
836 Eburnean geodynamic evolution of the gold-rich southern Ashanti Belt, Ghana, with new
837 field and geophysical evidence of pre-Tarkwaian deformations. Precambrian Res 204-
838 205:12-39

839 Philipps GN, Powell R (2010) Formation of gold deposits: a metamorphic devolatilization
840 model. J Metam Geol 28:689-718

841 Pouclet A, Doumbia S, Vidal M (2006) Geodynamic setting of the Birimian volcanism in
842 central Ivory Coast (western Africa) and its place in the Palaeoproterozoic evolution of
843 the Man Shield. B Soc Geol Fr 177:105-121

844 Robertson M, Peters L (2016) West African goldfields. Episodes 39:155-176

845 Rogers AJ, Kolb J, Meyer FM, Vennemann T (2013) Two stages of gold mineralization at Hutti
846 mine. *Miner Deposita* 48:99-114

847 Roux P, Lemarchand D, Hughes HJ, Turpault MP (2015) A Rapid Method for Determining
848 Boron Concentration (ID-ICP-MS) and $\delta^{11}\text{B}$ (MC-ICP-MS) in Vegetation Samples after
849 Microwave Digestion and Cation Exchange Chemical Purification. *Geostand Newslett*
850 39:453-466

851 Rowins SM, Groves DI, McNaughton NJ, Palmer MR, CS Eldridge (1997) A reinterpretation
852 of the role of granitoids in the genesis of Neoproterozoic gold mineralization in the Telfer
853 Dome, Western Australia. *Econ Geol* 92:133-160

854 Sciuba M, Beaudoin G, Makvandi S (2020) Chemical composition of tourmaline in orogenic
855 gold deposits. *Miner Dep* in press

856 Slack JF (1996) Tourmaline associations with hydrothermal ore deposits. In: Grew ES, Anovitz
857 LM (eds) *Boron, Mineralogy, Petrology and Geochemistry*. *Rev Mineral* 33:559-643

858 Slack JF, Trumbull RB (2011) Tourmaline as a Recorder of Ore-Forming Processes. *Elements*
859 7:321-326

860 Spear FS, Kohn MJ, Cheney JT (1999) P-T paths from anatectic pelites. *Contrib Mineral Petr*,
861 134:17-32

862 Thébaud N, Allibone A, Masurel Q, Eglinger A, Davis J, André-Mayer AS, Miller J, Jessell M
863 The Paleoproterozoic (Rhyacian) gold deposits of West Africa (2020, accepted, proof in
864 progress) *Econ Geology*

865 Thompson AB (1982) Dehydration melting of pelitic rocks and the generation of H₂O-
866 undersaturated granitic liquids. *Am J Sci* 282:1567-1595

867 Tomkins AG (2013) On the source of orogenic gold. *Geology* 41:1255-1256

868 Trumbull RB, Slack JF (2018) Boron isotopes in the continental crust: granites, pegmatites,
869 felsic volcanic rocks, and related ore deposits. In: Marschall HR, Foster GL (Eds), *Boron*

870 Isotopes – The Fifth Element. Advances in Isotope Geochemistry, Springer-Verlag, pp
871 249-272

872 Tshibubudze A, Hein KAA (2013) Structural setting of gold deposits in the Oudalan-Gorouol
873 volcano-sedimentary belt east of the Markoye Shear Zone, West African Craton. J Afr
874 Earth Sci 80:31-47

875 Tshibubudze A, Hein KAA, Marquis P (2009) The Markoye Shear Zone in NE Burkina Faso.
876 J Afr Earth Sci 55:245-256

877 van Hinsberg VJ, Henry DJ, Marschall HR (2011) Tourmaline: an ideal indicator of its host
878 environment. Can Mineral 49:1-16

879 Vegas N, Naba S, Bouchez JL, Jessell M (2008) Structure and emplacement of granite plutons
880 in the Paleoproterozoic crust of Eastern Burkina Faso: rheological implications. Int J
881 Earth Sci 97:1165-1180

882 Vielzeuf D, Holloway JR (1988) Experimental determination of the fluid-absent melting
883 relations in the pelitic system. Contrib Mineral Petr 98:257-276

884 von Goerne G, Franz G, Heinrich W (2001) Synthesis of tourmaline solid solutions in the
885 system Na₂O-MgO-Al₂O₃-SiO₂-B₂O₃-H₂O-HCl and the distribution of Na between
886 tourmaline and fluid at 300 to 700°C and 200 MPa. Contrib Mineral Petr 141:160-173

887 von Goerne G, Franz G, van Hinsberg VJ (2011) Experimental determination of Na-Ca
888 distribution between tourmaline and fluid in the system CaO-Na₂O-MgO-Al₂O₃-SiO₂-
889 B₂O₃-H₂O. Can Mineral 49:137-152

890 Vry J, Powell R, Golden KM, Petersen K (2010) The role of exhumation in metamorphic
891 dehydration and fluid production. Nat Geosci 3:31-35

892 Wang LG, McNaughton NJ, Groves DI (1993) An overview of the relationship between
893 granitoid intrusions and gold mineralization in the Archaean Murchison Province,
894 Western Australia. Miner Deposita 28:482-494

895 Wunder B, Meixner A, Romer RL, Wirth R, Heinrich W (2005) The geochemical cycle of
 896 boron: constraints from boron isotope partitioning experiments between mica and fluid.
 897 Lithos 84:206-216
 898 Wyman D, Kerrich R (1988) Alkaline magmatism, major structures, and gold deposits:
 899 implications for greenstone belt gold metallogeny. Econ Geol 83:454-461
 900 Xue Y, Campbell IH, Ireland TR, Holden P, Armstrong R (2013) No mass-independent sulfur
 901 isotope fractionation in auriferous fluids supports a magmatic origin for Archean gold
 902 deposits. Geology 41:791-794
 903 Yavuz F, Karakaya N, Yildirim DK, Karakaya MC (2014) A Windows program for calculation
 904 and classification of tourmaline-supergroup (IMA-2011). Comput Geosci 63:70-87
 905

Figure captions

Figure 1. A. Location and geological setting of the Kiaka orogenic gold deposit in the West African Craton (modified after Castaing et al. 2003; Naba et al. 2004; Milési et al. 2004; Vegas et al. 2008; Ganne et al. 2012). The Kénéma Man domain (Archean nucleus) and the Baoulé-Mossi domain (Paleoproterozoic juvenile crust) form two domains separated by the Sassandra Fault (SF). Volcano-sedimentary belts include Banfora (BA), Houndé (HO), Boromo (BO), Lawra (LW), Goren (GO), Bui (BU), Ashanti (AS) and Sefwi (SW), Haute Comoé basin (HC), and Manga Fada-N’Gourma belt (MFG). These belts are separated into dark green for mafic volcanics rocks and light green for volcano-sedimentary rocks and intermediate to felsic igneous rocks (Baratoux et al. 2011). A spatial association is found between gold deposits of the Baoulé-Mossi domain and major tectonic structures such as the Grenville-Ferkessedougou-Bobo-Dialouso (GFBF), Ouango-Fitini (OF) and Markoye (MSZ; this study) shear zones. For interpretation of the colors, the reader is referred to the web version of this article. **B.** Geology of the Manga Fada-N’Gourma greenstone belt with MSZ (thick black lines) and location of the Kiaka gold deposit (Fontaine et al. 2017). **C.** Local geology of the Kiaka deposit showing the location of the drillholes and cross-sections. Mineralized envelopes are projected at surface from drillhole data (modified from Fontaine et al. 2017). **D.** NW-striking section 6100 showing the location of the diorite plug.

Figure 2. Paragenetic sequence of the Kiaka gold deposit and relationships with the structural events and hydrothermal alteration.

Figure 3. Mineralogical and textural features of tourmaline in the alteration zones of the Kiaka gold deposit. **A & B.** Muscovite schist containing folded garnet-biotite-chlorite-muscovite layer

with detrital tourmaline (*Tur₁*) (sample KDH75-64.9). **C & D.** Metagreywacke composed of quartz, plagioclase, and biotite, containing disseminated tourmaline and clinozoisite (sample KDH29-311.8). **E & F.** Metamafic rock-hosted tourmaline porphyroblasts (*Tur₂*) associated with D₂Ki biotite-clinozoisite-titanite-pyrrhotite alteration assemblage and crosscut by chlorite (Chl 3)-calcite D₄Ki veinlet (sample KDH291-56.2). Mineral abbreviations: Bt=biotite, Cal=calcite, Chl=chlorite, Czo=clinozoisite, Kfs=K-feldspar, Grt=garnet, Ms=moscovite, Qtz=quartz, Pl=plagioclase, Po=pyrrhotite, Ttn=titanite, Tur=tourmaline.

Figure 4. Petrography of hydrothermal tourmaline (*Tur₂*) hosted in metagreywacke (sample KDH29-311.8). **A.** Backscattered electron images of euhedral grains of hydrothermal tourmaline in an assemblage of quartz, biotite, K-feldspar, and pyrrhotite. Note the homogeneity of the tourmaline grains. **B.** Plane-polarized transmitted-light photomicrograph of hydrothermal tourmaline grains.

Figure 5. Petrography of metamafic rock-hosted hydrothermal tourmaline (*Tur₂*) porphyroblasts (sample KDH291-56.2). **A.** Global view of the three studied tourmaline porphyroblasts (Grain 1, Grain 2, and Grain 3) observed by plane-polarized transmitted light (x150) and **B.** interpretation sketch below (modified after Fontaine et al. 2017). The hydrothermal assemblage is cut by a D₄Ki calcite-chlorite vein. **C.** Backscattered electron image of a tourmaline porphyroblast (Grain 2) showing complex zoning and numerous sulfide inclusions.

Figure 6. X-ray elemental maps of a poikilitic tourmaline porphyroblast (*Tur₂*, Grain 2) hosted in metamafic rock (sample KDH291-56.2). **A** and **B** show the tourmaline grain in transmitted

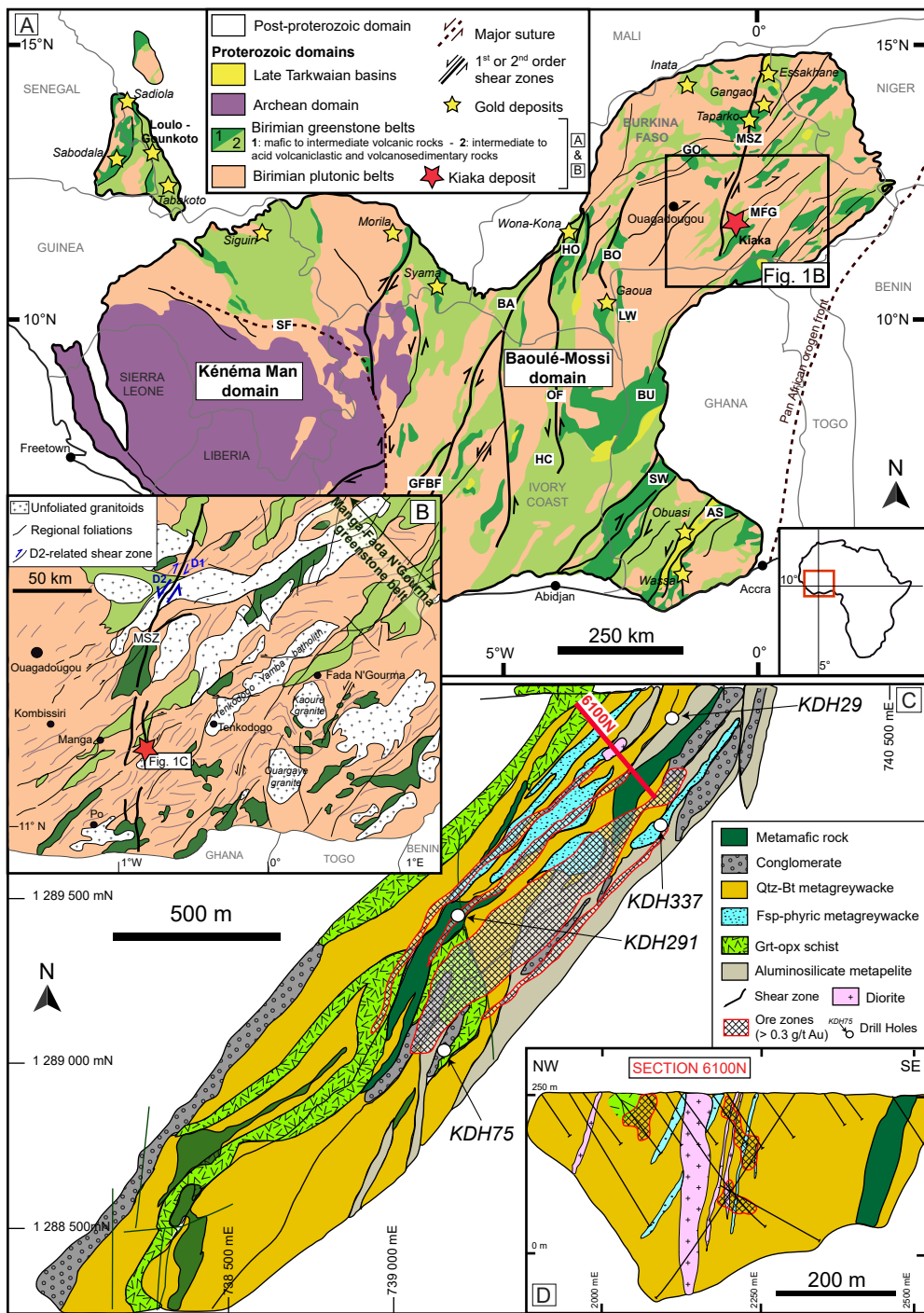
light (TL) and backscattered electrons (BSE) (same as Figure 5C). Relative intensities of the elements Fe, Mg, Al, Ca, Na, and Ti (C, D, E, F, and G) are shown with count/sec. scales.

Figure 7. Chemical compositions of hydrothermal tourmaline (*Tur*₂) hosted in metamafic rock (sample KDH291-56.2) and metagreywacke (sample KDH29-311.8). **A.** Binary diagram $X_{\text{vacancy}}/(X_{\text{vacancy}}+\text{Na})$ vs. $\text{Mg}/(\text{Fe}+\text{Mg})$, indicating that *Tur*₂ belongs to domain dravite/oxydravite. **B.** Binary diagram Fe vs. Mg, showing low Mg composition for metagreywacke-hosted *Tur*₂, and a richer Mg content for *Tur*₂ hosted in metamafic volcanic rock. **C.** Binary diagram X_{vacancy} vs. Al, showing a dravite-schorl composition for metamafic rock tourmaline, and a composition closer to foitite/magnesio-foitite for metagreywacke tourmaline. **D.** Binary diagram Fe vs Al, highlighting higher Al content for metagreywacke tourmaline compared to metamafic rock tourmaline. **E.** Ternary diagram Ca- X_{vacancy} -(Na+K) illustrating the belonging of *Tur*₂, for both lithologies, to the alkali group. **F.** Ternary diagram Al-Fe-Mg. The numbered fields in the Al-Fe-Mg diagram correspond to the compositional range of tourmaline hosted in different rock types as defined by Henry and Guidotti (1985): 1- Li-rich granitoids, pegmatites and aplites; 2- Li-poor granitoids, pegmatites and aplites; 3- Fe^{3+} -rich quartz-tourmaline rocks (hydrothermally altered granitoids); 4- Al-rich metapelites and metapsammites; 5- Al-poor metapelites and metapsammites; 6- Fe^{3+} -rich quartz-tourmaline rocks, calc-silicate rocks and metapelites; 7- Low-Ca meta-ultramafic rocks and Cr-V-rich metasediments; 8- Metacarbonates and metapyroxenites.

Figure 8. Boron isotope compositions of hydrothermal tourmaline (*Tur*₂) from the Kiaka gold deposit. **A.** Histogram showing the $\delta^{11}\text{B}$ distribution of tourmaline hosted in metamafic rock (sample KDH291-56.2) and metagreywacke (sample KDH29-311.8) compared to the whole-rock $\delta^{11}\text{B}$ compositions of the diorite (sample KDH337-44.1) and the muscovite schist (sample KDH75-64.9). **B.** $\delta^{11}\text{B}$ compositional range of tourmaline from orogenic gold deposits

worldwide. Data are compiled from (1) Lambert-Smith et al. (2016); (2) Molnár et al. (2016); (3) Krienitz et al. (2008); (4, 5) Jiang et al. (2002); (6) Beaudoin et al. (2013); (7, 8, 9) Baksheev et al. (2015). C. $\delta^{11}\text{B}$ compositional range of tourmaline hosted in variable lithologies worldwide (Marschall and Jiang 2011; Trumbull and Slack 2018).

Figure 9. Boron isotope fractionation curves between tourmaline and fluid for a stepwise decreasing temperature from 650 to 350°C (after Büttner et al. 2016). The isotopic composition of fluid and tourmaline are calculated for a starting initial fluid composition of $\delta^{11}\text{B} = -21.5\text{‰}$ using the Rayleigh fractionation model of Marschall et al. (2009) and the temperature-dependent tourmaline-fluid fractionation values of Meyer et al. (2008).

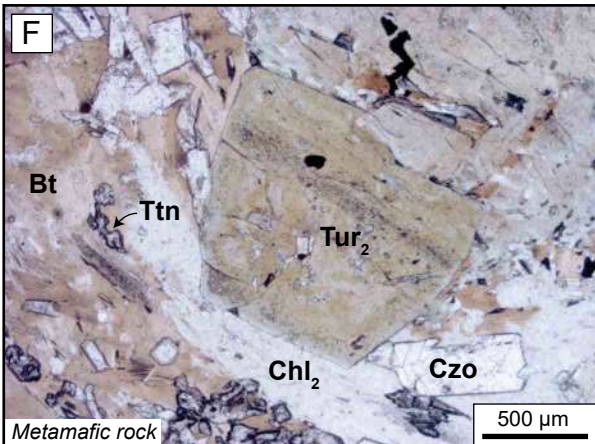
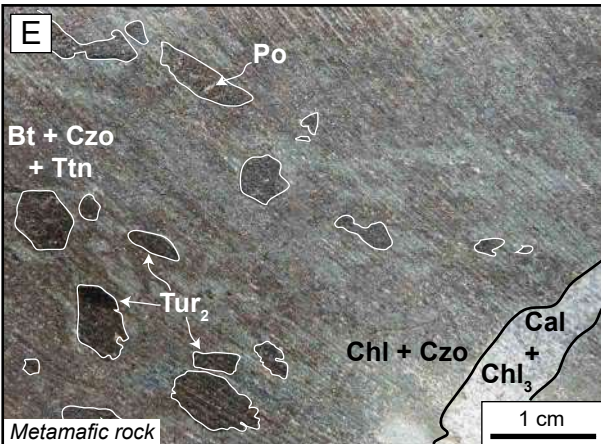
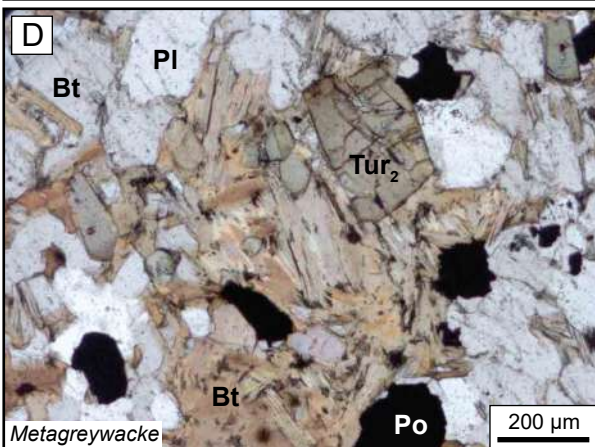
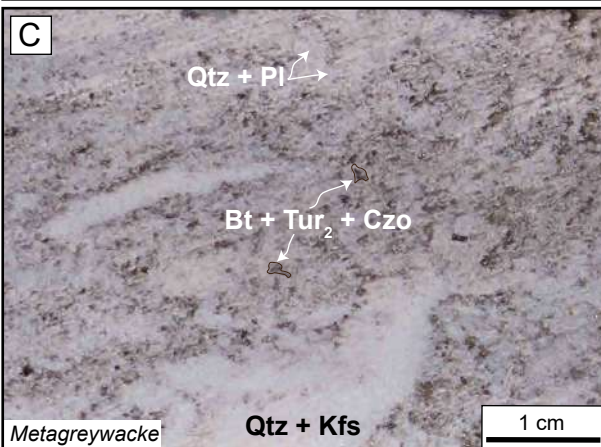
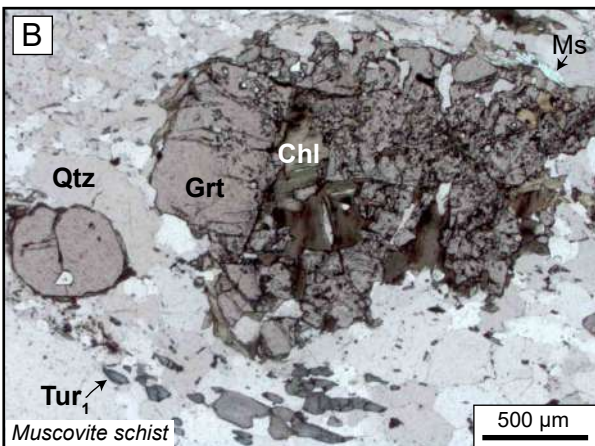
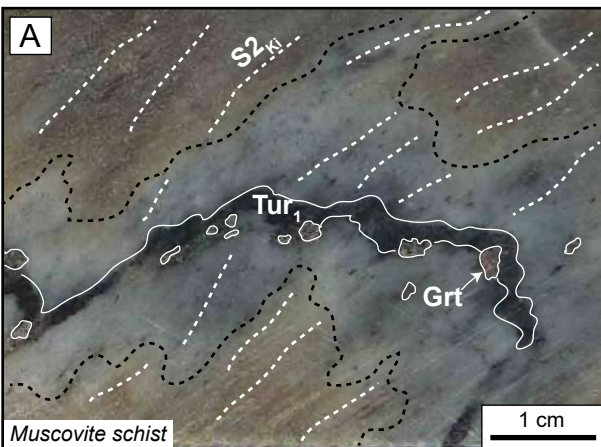


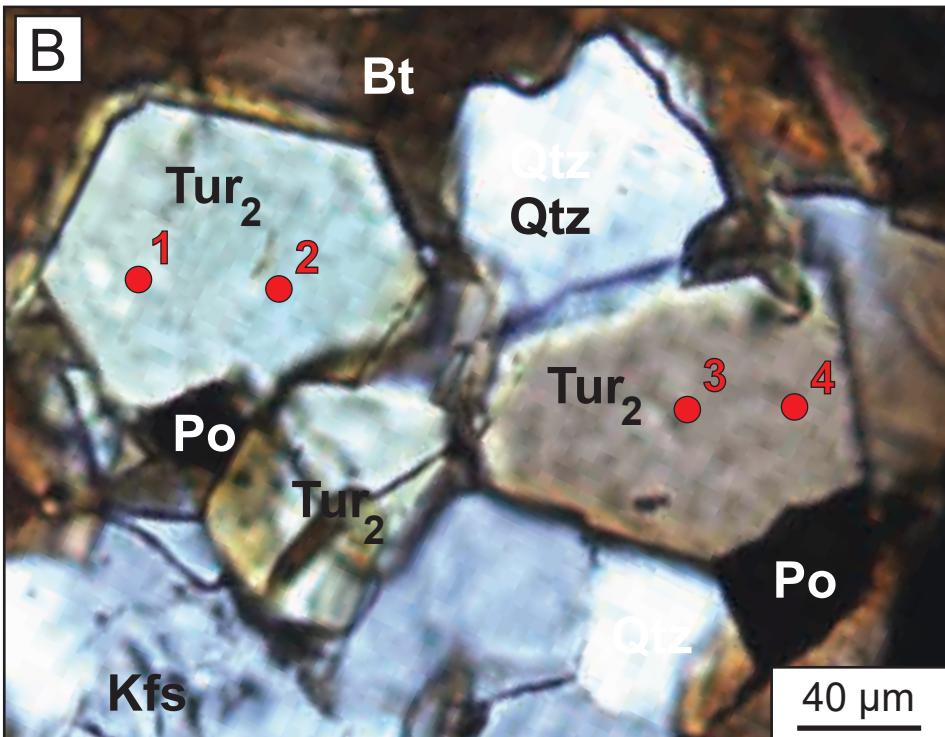
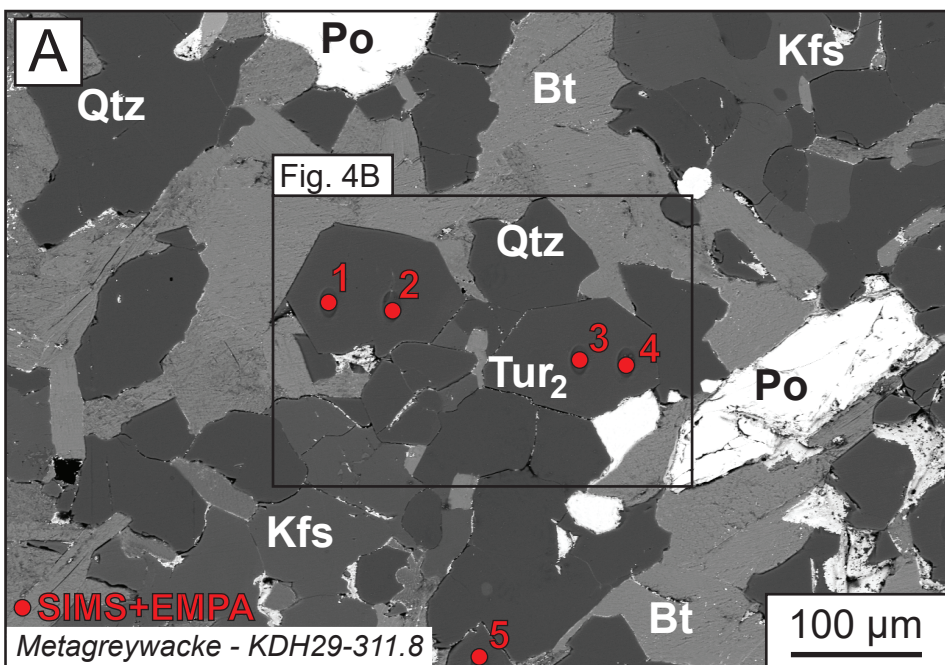
Deformation	D1	SYN-D2	LATE-D2	D3	D4
Metamorphism	Prograde	Prograde (7.5 kbar; 550°C) Diorite emplacement and shearing		D3 _{Kf} -D4 _{Kf} events Retrograde Reactivation of D2 shearzones	
Tourmaline generation					
<i>Tur</i> ₁ : Detrital Rounded, brown to blue ^{1,2} <u>with Grt, Bt and Ms</u>					
<i>Tur</i> ₂ : Hydrothermal Euhedral brown, inclusion-poor ¹ Poikiloblastic mm and inclusion-rich ³		<u>with Ap, Qtz and Po inclusions</u> <u>with Po, Ccp, Chl, Czo and Act inclusions</u>			
Mineralization					
Po ± (Py, Ccp) disseminations in Bt replacement zones (1-3 g/t Au) ¹					
Apy ± (Lo) disseminations and Qz veinlets ¹					
Po ± (Py) in calc-silicate hydrothermal breccia					
Visible Au in Qtz-carbonate veinlets (50-60 g/t Au)					
Alteration					
Biotitization ^{1,3}					
Calc-silicate alteration ³					
Tourmalinization ^{1,3}					
Sericitization					
Chloritization ³ <u>Chl</u> ₁				<u>Chl</u> ₂	<u>Chl</u> ₃
Carbonatation					

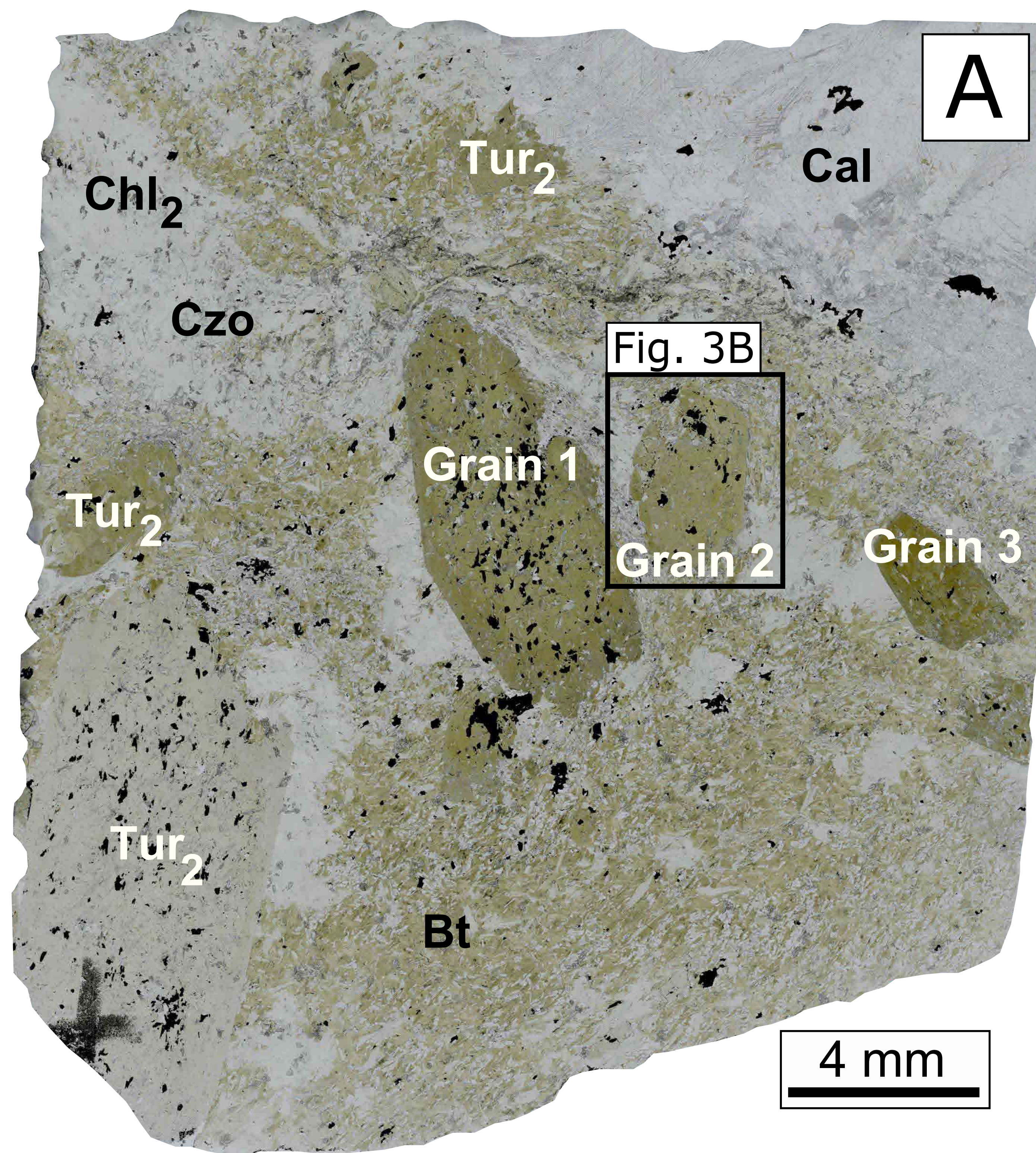
Major
 Minor
 Rare

¹ mainly in aluminosilicate-bearing metapelites and quartz-biotite metagreywacke
² mainly in quartz-muscovite schist
³ mainly in metamafic rock

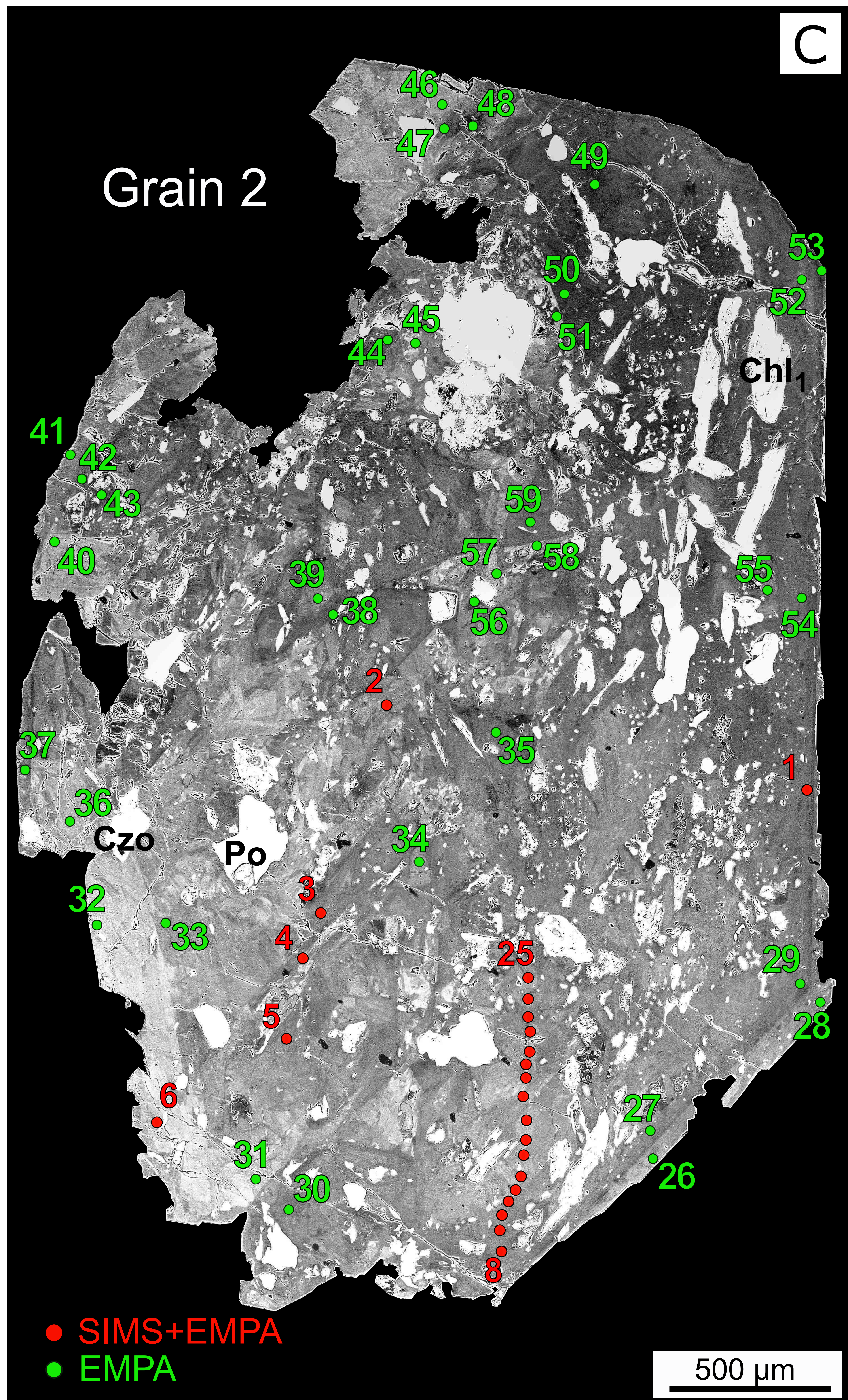
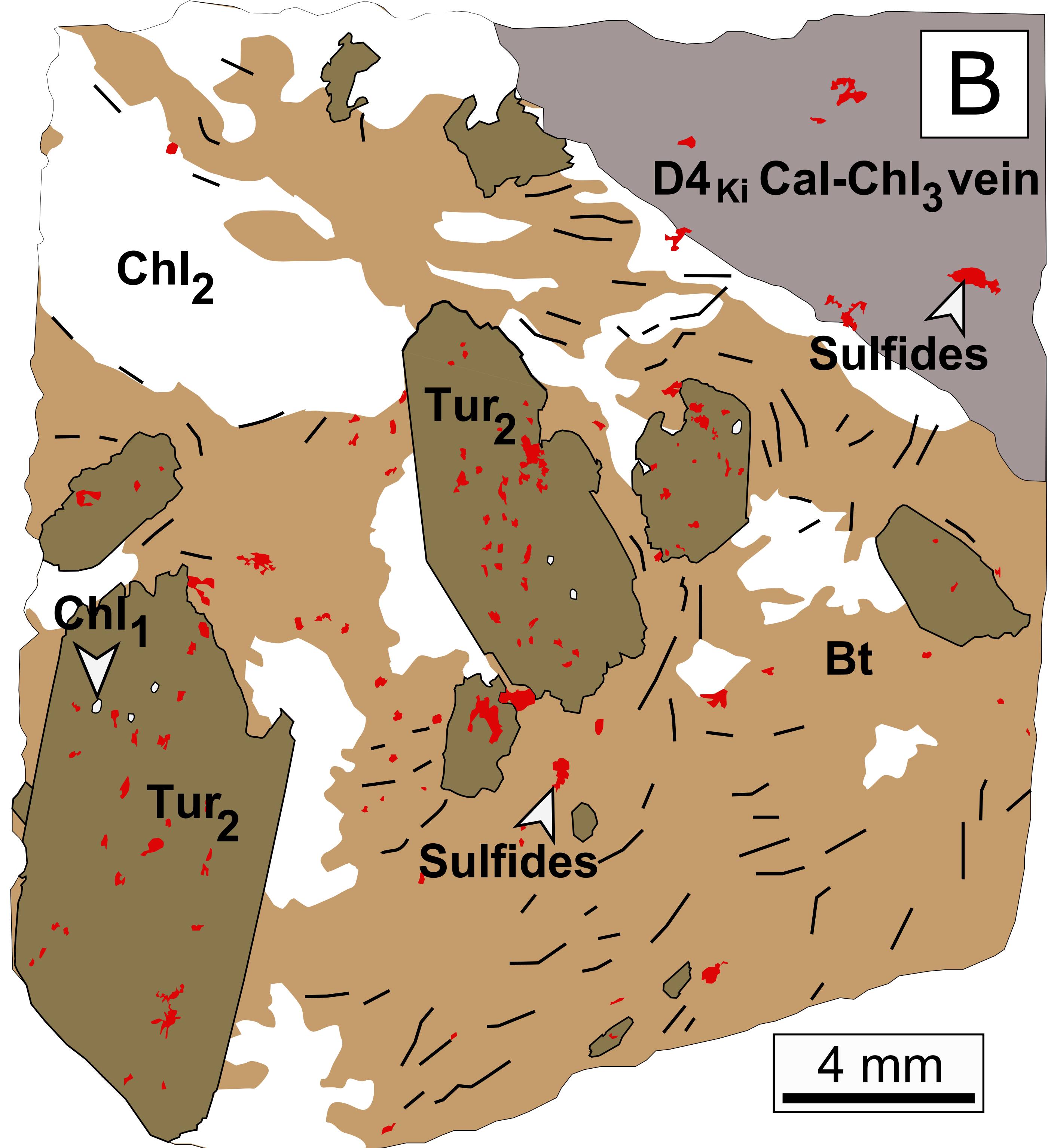
Deformation	D1	SYN-D2	LATE-D2	D3	D4
Metamorphism	Prograde	Prograde (7.5 kbar; 550°C) Diorite emplacement and shearing		D3 _{K1} -D4 _{K1} events Retrograde Reactivation of D2 shearzones	
Tourmaline generation					
<i>Tur₁</i> : Detrital Rounded, brown to blue ^{1,2} . <u>with Grt, Bt and Ms</u> .					
<i>Tur₂</i> : Hydrothermal Euhedral brown, inclusion-poor ¹ Poikiloblastic mm and inclusion-rich ³	<u>with Ap, Qtz and Po inclusions</u>		<u>with Po, Ccp, Chl, Czo and Act inclusions</u>		
Mineralization					
Po ± (Py, Ccp) disseminations in Bt replacement zones (1-3 g/t Au) ¹	_____				
Apy ± (Lo) disseminations and Qz veinlets ¹	_____				
Po ± (Py) in calc-silicate hydrothermal breccia	-----				
Visible Au in Qtz-carbonate veinlets (50-60 g/t Au)	_____				
Alteration					
Biotitization ^{1,3}	_____				
Calc-silicate alteration ³	-----				
Tourmalinization ^{1,3}	_____				
Sericitization	-----				
Chloritization ³	<u>Chl₁</u> -----		----- <u>Chl₂</u> ----- <u>Chl₃</u> -----		
Carbonatation	-----				
<div> <div>_____</div> Major <div>-----</div> Minor <div>-----</div> Rare </div> <div> ¹ mainly in aluminosilicate-bearing metapelites and quartz-biotite metagreywacke ² mainly in quartz-muscovite schist ³ mainly in metamafic rock </div>					

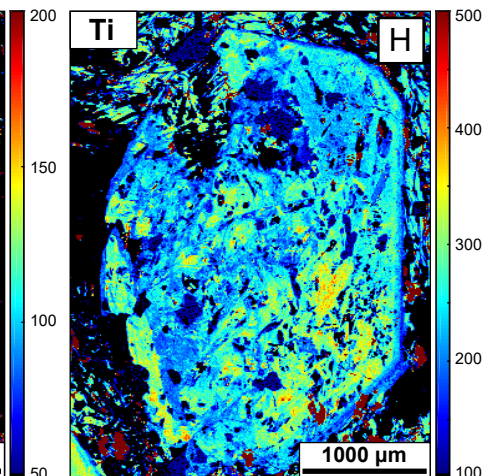
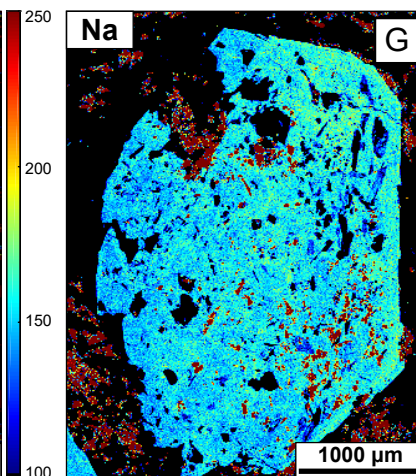
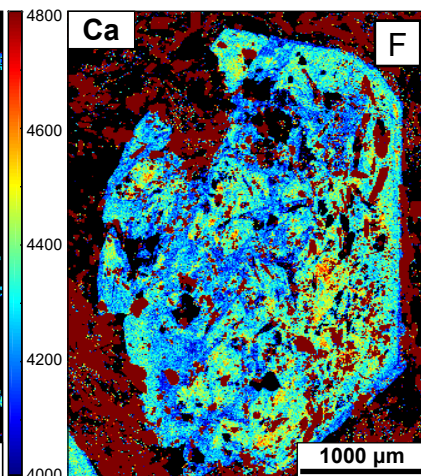
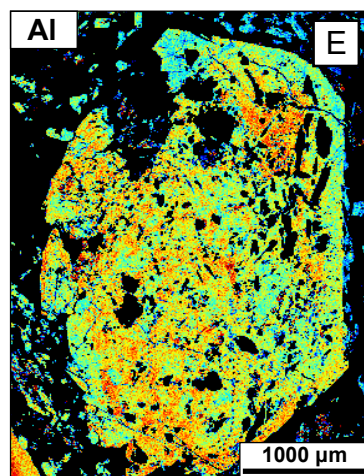
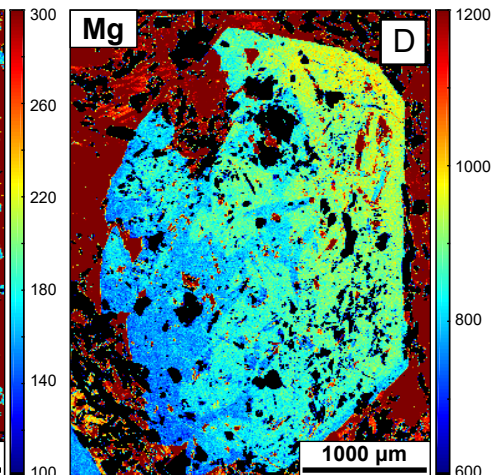
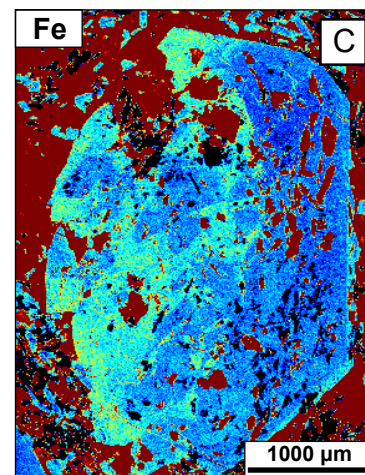
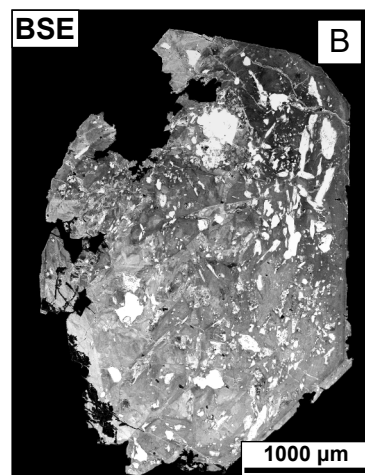
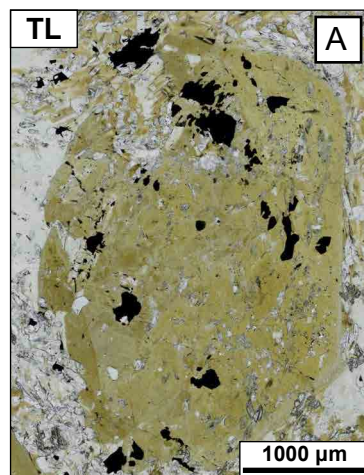


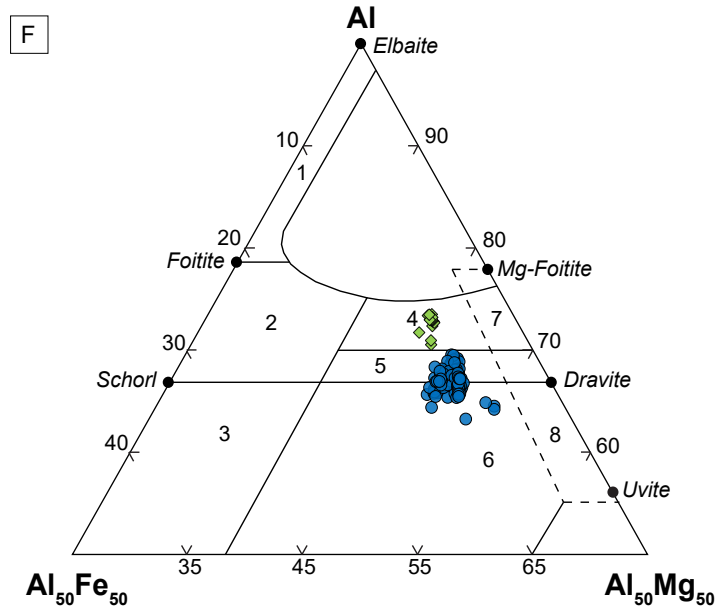
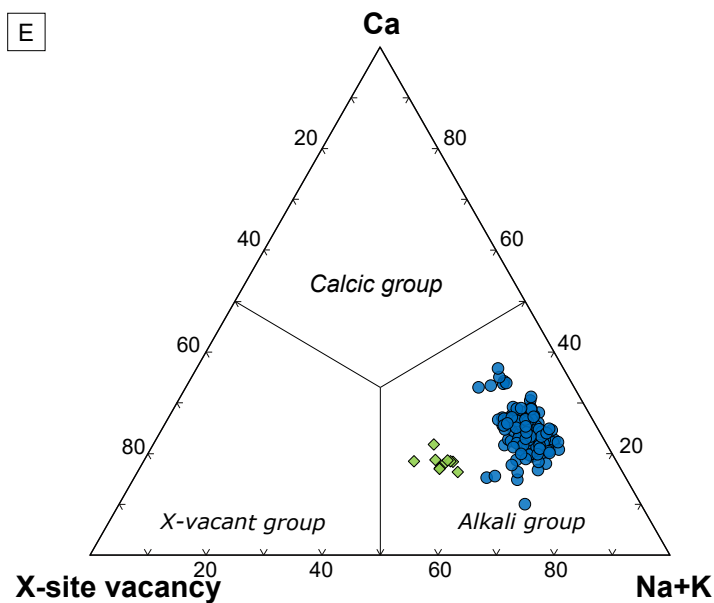
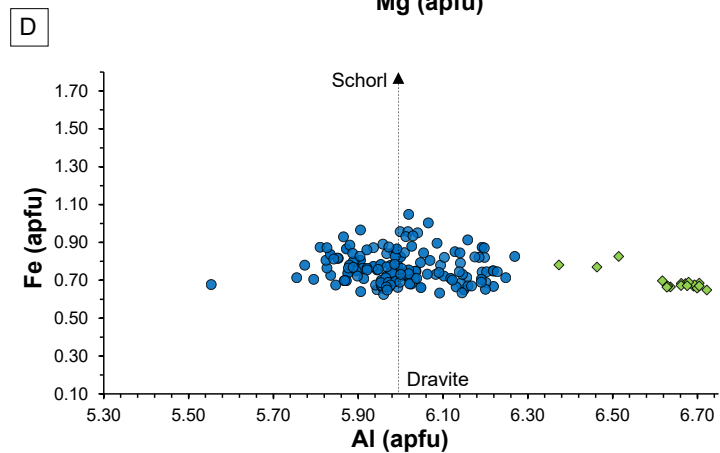
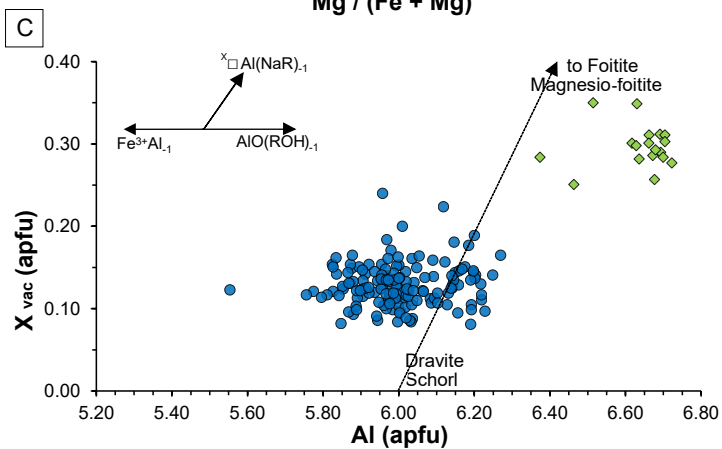
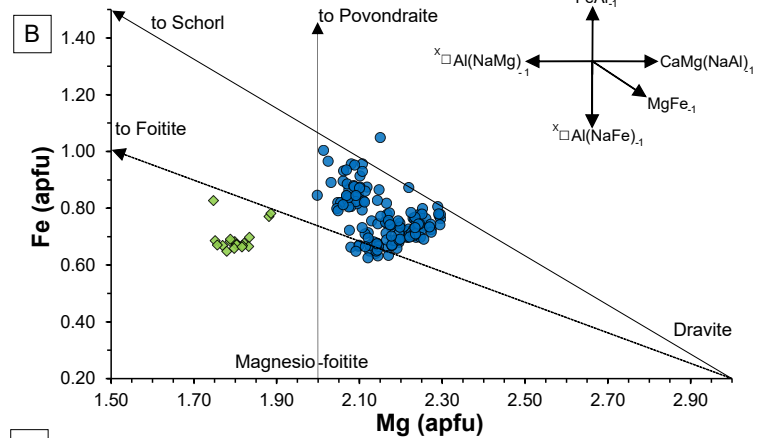
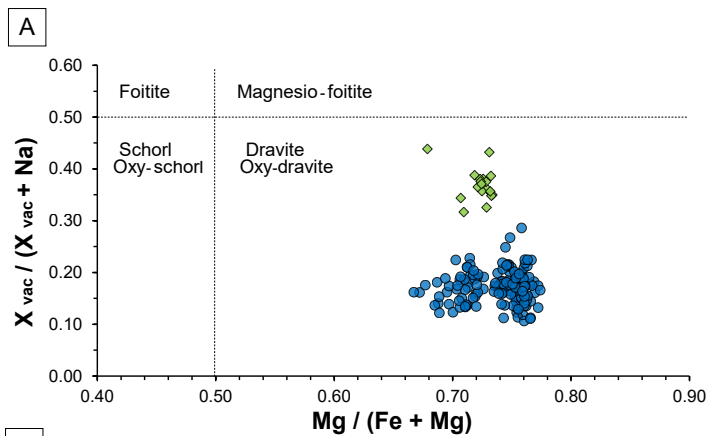




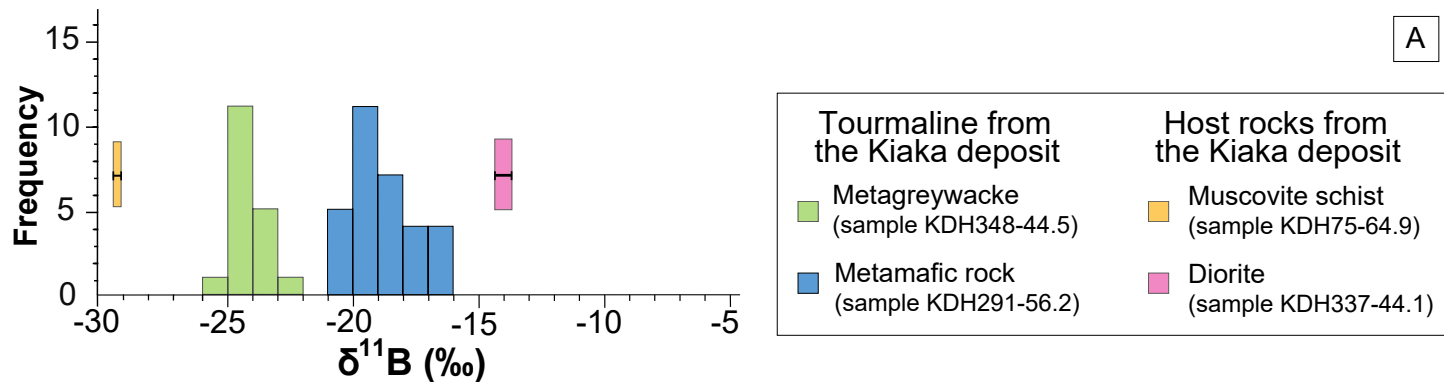
Metamafic rock - KDH291-56.2



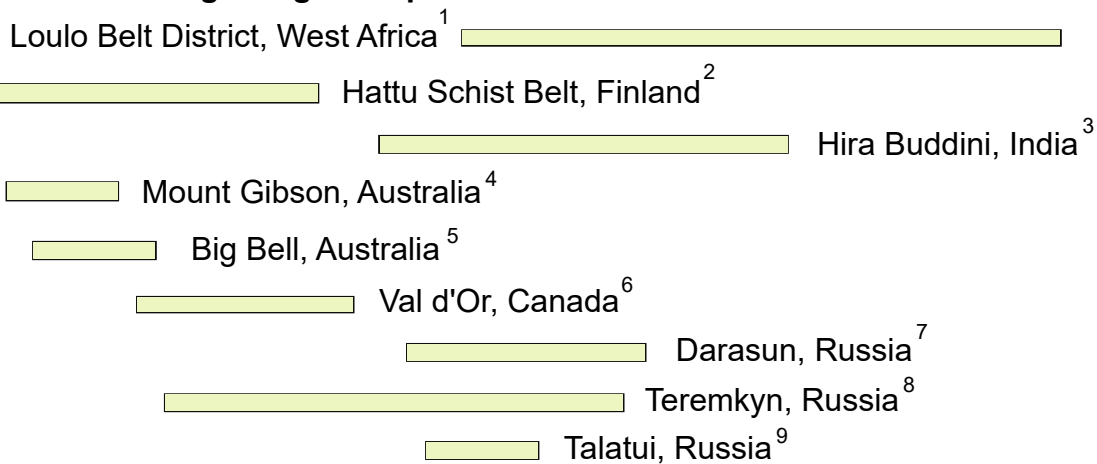




● Metamafic rock (sample KDH291-56.2)
 ◆ Metagreywacke (sample KDH29-311.8)



$\delta^{11}\text{B}$ of tourmaline from orogenic gold deposits



$\delta^{11}\text{B}$ of tourmaline hosted in...

